Building and Environment 262 (2024) 111842

Contents lists available at ScienceDirect

Building and Environment

journal homepage: www.elsevier.com/locate/buildenv

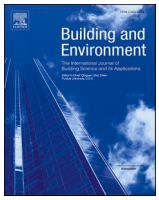

The similitude of indoor airflow in natural ventilation for a reduced-scale model: Investigation of nonisothermal flow fields by RANS simulation

Zitao Jiang [a,*], Tomohiro Kobayashi [a], Toshio Yamanaka [a], Mats Sandberg [b], Haruna Yamasawa [a], Miyazawa Shohei [a]

[a] Department of Architectural Engineering, Graduate School of Engineering, Osaka University, Osaka, Japan
[b] Department of Building Engineering, Energy Systems and Sustainability Science, University of Gävle, Gävle, Sweden

ARTICLE INFO

Keywords:
Similarity
Natural ventilation
Buoyant flow
Reynolds number independence
Computational fluid dynamics (CFD)

ABSTRACT

Reduced-scale experiments and simulations are important approaches in natural ventilation research, and the similarity requirement is fundamental for generalising the flow characteristics obtained from reduced-to full-scale conditions. However, the similarity requirement of a nonisothermal natural ventilation flow in a reduced-scale model poses additional challenges because of the reduced approaching flow, which can potentially result in Reynolds dependence issues. This study investigated the Reynolds number (*Re*) independence of indoor airflow in natural ventilation under isothermal and nonisothermal conditions using computational fluid dynamics (CFD) with Reynolds-averaged Navier–Stokes. A wind tunnel experiment was first conducted to validate the accuracy of the CFD using a reduced-scale model. Indoor airflow fields characterised by the same Archimedes number (*Ar*) but with varying approaching wind velocities and temperatures were compared between the full-scale and 1/10 reduced-scale simulations. The dimensionless ventilation rate showed the least dependence on the Re number, while the temperature field was very sensitive to the Re number, especially in the near-wall region. However, the temperature field on the ventilation pathway is much less dependent on the Re number, the deviation of which is less than 10 % compared to the full-scale simulation. The temperature distribution in the reduced-scale simulation exhibits a thermal stratification pattern similar to that in the full-scale simulation.

1. Introduction

In recent years, there has been a growing emphasis on promoting and incorporating natural ventilation into architectural design and construction with the aim of fostering a built environment that is both healthier and more sustainable. The design optimisation of natural ventilation systems promotes energy efficiency [1–5], enhances indoor air quality [6–8], reduces the risk of Sick Building Syndrome [9–11], and improves thermal comfort [12–14].

Utilising natural ventilation systems to the fullest extent also necessitates effective methodologies for studying and understanding the dynamics of natural ventilation. Three primary methodologies were employed to investigate the flow field and performance of natural ventilation [15]: on-site measurements, reduced-scale experiments in laboratory settings (such as wind tunnel and water flume experiments), and computational fluid dynamics (CFD).

Full-scale on-site measurements, which provide the most reliable results that mirror the cumulative impact of various real-world factors without the constraints of similarity criteria [16–19], are rarely employed in research. This rarity can be attributed to inherent drawbacks, including high time and material costs, lack of repeatability, impracticality in the building design stage, and difficulty in conducting parametric studies.

In contrast to full-scale experiments, laboratory experiments offer several advantages, including repeatability, applicability at the building design stage, and the ability to control environmental parameters. The predominant focus of reduced-scale studies on natural ventilation in atmospheric boundary layer wind tunnels has been isothermal conditions [20–25]. However, studies on the thermal effects of natural ventilation are limited. Several studies have employed reduced-scale models in wind tunnels without considering the impact of atmospheric boundary layer wind flow [26,27], or conducted experiments within water flumes [28–30]. Laboratory experiments using a reduced-scale model have several purposes, including the exploration of

* Corresponding author.
E-mail address: jiang_zitao@arch.eng.osaka-u.ac.jp (Z. Jiang).

https://doi.org/10.1016/j.buildenv.2024.111842
Received 29 March 2024; Received in revised form 11 July 2024; Accepted 12 July 2024
Available online 17 July 2024

fundamental natural ventilation flow structures, assessment of ventilation performance, and provision of validation datasets for CFD simulations or theoretical models.

The reduced-scale model is also used in numerical simulations. Ai et al. [31] proposed the use of reduced-scale models for the computation of wind flow fluid dynamics simulations. Both the theoretical and simulation results support the idea that a reduced-scale model can provide good prediction accuracy with much fewer computational resource requirements than a full-scale model, because the reduced-scale model requires fewer cells to achieve the $y+$ requirement. The reduced-scale numerical water-tank approach was also developed to study urban-scale buoyancy-driven flow [32,33].

The fundamental requirement for the reduced-scale experiment and simulation is the similarity criteria, which requires to replicate certain nondimensional parameters from the prototype in the model, and it guarantees that the conclusion obtained from a reduced-scale experiment can be generalised and scaled into full-scale conditions. Snyder [34,35] systematically performed a similarity analysis of atmospheric fluid motions and four significant nondimensional parameters are summarised to determine the flow patterns: the Reynolds number (*Re*), Rossby number (*Ro*), Peclet number (*Pe*), and Froude number (*Fr*). It is generally impossible and unnecessary to use all the nondimensional parameters in a reduced-scale experiment [34–36]. Snyder [34] indicated that the Rossby number should only be considered when simulating prototype flows with length scales exceeding 5 km. Aligning the Reynolds, Peclet, or Schmidt numbers is not necessary if the Reynolds number of the flow is high. Consequently, when modelling the isothermal flow in natural ventilation, it is essential to consider only *Re*. However, under nonisothermal conditions, both Re and *Fr* should be considered.

Re is defined as the ratio of inertial force to viscous force:

$$Re = \frac{UL}{\upsilon} \tag{1}$$

where U is the characteristic velocity (m/s), L is the characteristic length (m), and υ is the kinematic viscosity (m^2/s). U and L are determined for a specific problem of interest. For airflow within building blocks and street canyons, the commonly adopted parameter is the building Reynolds number (Re_H) [37–39], which utilises the building height and wind speed at the roof level as reference values. In cases of indoor airflow in natural ventilation, the opening Reynolds number (Re_o) is defined using the size of the opening and the mean velocity through the opening [40,41]. In the present study, Re_o is adopted because the airflow through the opening largely influences the indoor airflow pattern in natural ventilation, and Re_o is defined as follows:

$$u_o = \frac{Q}{A} \tag{2}$$

$$L = \frac{4A}{P} = \frac{4ab}{2(a+b)} = \frac{2ab}{a+b} \tag{3}$$

$$Re_o = \frac{u_o L}{\nu} = \frac{2Q}{\nu(a+b)} \tag{4}$$

where Q is the ventilation rate (m^3/s); u_o is the mean velocity at the opening (m/s); A is the opening area (m^2); L is the hydraulic diameter (m); and a and b are the length and width of the opening (m), respectively. In reduced-scale experiments focusing on natural ventilation, the model scale is mainly determined by the blockage ratio requirement of a maximum of 5 % of the wind tunnel working section [42]; thus, a typical scale ratio of 1:10–1:100 is usually employed. Nevertheless, achieving precise matching of the Re in such reduced-scale experiments necessitates a substantial increase, by a factor of 10–100, in the approaching wind velocity condition, which is challenging to attain in wind tunnel experiments. Many previous studies have attempted to justify the use of a smaller Re in reduced-scale experiments; this is known as the Reynolds independence problem [34]. Townsend [43] proposed the Reynolds-number independence hypothesis, which states that the primary flow and turbulence structure are independent of the Reynolds number for sharp-edged geometries if the Reynolds number is sufficiently high. The threshold of the required Reynolds number is known as the critical Reynolds number.

The critical Re value for Reynolds independence has been extensively investigated and discussed for external flows at the urban scale [38,39,44,45]. Nevertheless, there is much less investigation of the Reynolds independence in the indoor airflow of natural ventilation. Dai et al. [37] performed CFD to investigate the *Re*-independence criteria of isothermal flows in reduced-scale isolated buildings and building arrays with single-opening ventilation. The simulation suggested that the *Re*-independence requirement is $Re_o = 14,000$, $Re_o = 30,000$ for the indoor airflow fields and pollutant concentrations, respectively. In terms of nondimensional ventilation rates in each room, the critical values were $Re_o = 10,000$, $Re_o = 13,000$ for the indoor airflow fields and pollutant concentrations, respectively. Cui et al. [40] studied the *Re*-independence issues of cross ventilation in an isolated building using CFD. The results indicated that the critical Re_o value for indoor airflow is $Re_o = 15,000$ and that cross ventilation was independent of the window size. Cui et al. [41] further investigated the *Re*-independence problem of cross- and single-opening ventilation under isolated and sheltered building conditions. The results show that the indoor airflow pattern can be better characterised by Re_o than by Re_H. Moreover, under the same approaching flow, it is more difficult for the flow structure of single-opening ventilation to be *Re*-independent compared to cross ventilation, while the critical Re_o is independent of the ventilation modes and surrounding building effects.

The driving forces of natural ventilation can be classified into wind- and buoyancy-induced forces [46,47]. Buoyancy-induced ventilation is widely used in high-rise buildings and large public buildings with considerable height differences between the inlet and outlet openings. Neves et al. [48] performed simulations and measurements of wind force (wind speed and direction) and buoyancy force (solar radiation) on the solar chimney performance of a reduced-scale model; the results revealed that the airflow rate and airflow pattern were affected by thermal gradients, outdoor wind velocity, and direction. Liu et al. [49] investigated winter air infiltration induced by combined buoyancy and wind forces in a large-space building and proposed a simplified method to predict the winter air infiltration rate in large-space buildings. When conducting reduced-scale experiments or simulations for nonisothermal flows induced by combined wind and buoyancy forces, both Re and *Fr* should be considered. The Richardson number (*Ri*), which is the inverse of the square of *Fr*, is widely used to describe buoyant flows [50–53]:

$$Ri = \frac{\Delta\rho g L}{\rho U^2} \tag{5}$$

where $\Delta\rho$ is the air density difference (kg/m^3), g is the gravitational acceleration (m/s^2), L is the characteristic length (m), and U is the characteristic velocity (m/s). A similar definition [36,54] is also frequently referred to as Archimedes number (*Ar*):

$$Ar = \frac{U_b^2}{U_w^2} = \frac{\Delta\rho g h}{\rho U_w^2} = \frac{1}{Fr}\frac{\Delta\rho}{\rho} = \frac{1}{Fr}\frac{\Delta T}{T} \tag{6}$$

where U_b is the buoyancy velocity ($U_b = \sqrt{\Delta\rho g h/\rho}$, m/s), h is the vertical distance between two openings (m), U_w is the reference wind velocity (m/s), and *Fr* is defined as gh/U_w^2. The expression of *Ar* is widely used in indoor ventilation research [55–57]. Because the present study focuses on indoor ventilation flow patterns, it is hereinafter referred to as *Ar*. For a reduced-scale experiment or simulation of natural ventilation with both wind and buoyancy forces, *Ar* in the reduced-scale experiment should match that in the full-scale experiment. For

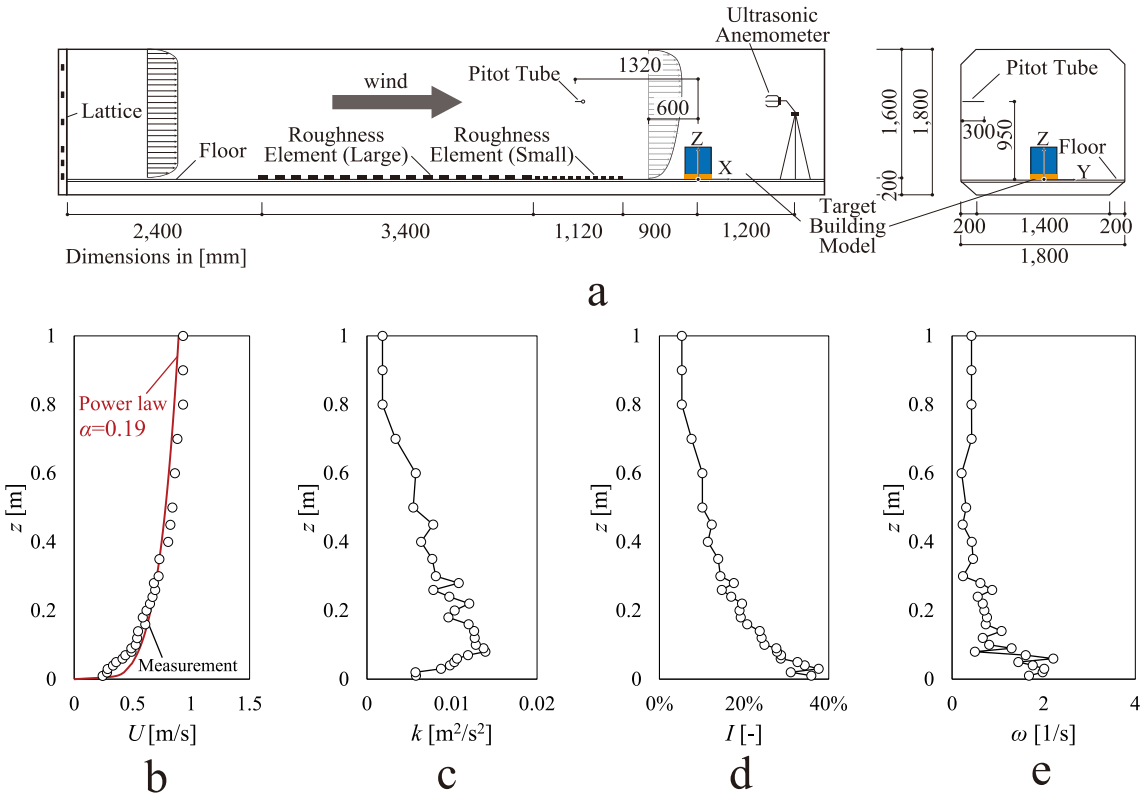

Fig. 1. (a) Wind tunnel schematic diagram. (b) Profiles of mean velocity U. (c) Profiles of turbulent kinetic energy k. (d) Profiles of turbulence intensity I. (e) Profiles of turbulence-specific dissipation rate ω.

example, for a full-scale building with $\Delta T = 5K$, the ΔT in a 1:10 reduced-scale model should be 50 K if the approaching flow has the same magnitude as the full-scale approaching flow, which makes the temperature difference very challenging to achieve. If the velocity in reduced scale can be decreased to half of that in full scale, then the $\Delta T = 12.5K$ in reduced scale can satisfy the Ar requirement. However, a lower approaching flow speed leads to a lower Re, which may not satisfy the Re-independence requirement of indoor airflow.

Chew et al. [52] investigated the Re and Ar similarities of buoyant flows in street canyons using CFD. He pointed out that even with the same order of Ar at reduced scale and full scale, the thermal effects are significant only at the reduced scale, which underscores the necessity of checking the Re-independence criterion for buoyancy-induced flow. Cui et al. [50] conducted a series of wind tunnel measurements on the thermal effects of airflow at different scales. The measurement manifests if the airflow in the street canyon achieves the Re-independence requirement and Ar becomes the only requirement for the flow pattern and temperature distribution of the external flow. A series of coupled CFD analyses performed by Cui et al. [51] also validated that if the requirement critical Re is reached, the airflow in the street and indoors at a reduced scale can represent a full-scale airflow pattern. Hwang et al. [58] performed a large-eddy simulation of a full-scale naturally ventilated single-room home with an identical Ar but varying wind speeds and temperatures. The results indicated that the nondimensional ventilation rate was strongly dependent on the ventilation Ar. Although Ar is widely used to characterise buoyant flows in outdoor wind flow studies [59], to the best of our knowledge, the influences of Re and Ar on the nonisothermal indoor airflow of natural ventilation have not been well investigated.

In addition to the flow pattern of natural ventilation, the ventilation rate is the other primary interest of natural ventilation, which is also correlated with Re and Ar. The ventilation rate of a room with two same-sized openings at different heights and assisting wind with buoyant flows can be calculated as follows:

$$Q = C_d A_{eff} \sqrt{\frac{2}{\rho}\left(\frac{1}{2}\rho U_w^2 \Delta Cp + \Delta \rho g h\right)} \tag{7}$$

where Q is the ventilation rate (m^3/s), C_d is the discharge coefficient (−), A_{eff} is the effective opening area (m^2), ρ is the air density (kg/m^3), U_w the characteristic wind velocity (m), ΔCp is the mean wind pressure coefficient difference between two openings (−), and h is the height difference between two openings (m). The dimensionless ventilation rate was normalised by the characteristic velocity and effective opening area, as follows:

$$Q^* = \frac{Q}{U_w A_{eff}} = C_d \sqrt{\Delta Cp + 2Ar} \tag{8}$$

where Ar is Archimedes' number. It should be noted that considering the similarity of nonisothermal indoor airflow fields, the wind speed should be the average wind speed at the opening. For the sake of simplicity, this study adopts the building height velocity (U_w) in the approaching flow, ensuring that the reference velocity for parameters such as ΔCp and Ar remains consistent. According to this equation, if Ar is the same, the dimensionless ventilation rate Q^* is only determined by C_d and ΔCp. In fully turbulent flow, if the building and openings are sharp-edged, the C_d and ΔCp are both independent of Reynolds values [15,54] which makes this equation extremely useful in predicting the ventilation rate at full scale. However, ΔCp depends on the building scale Reynolds number Re_H, and C_d depends on the opening scale Reynolds number Re_o if Re is low [54,60], and this problem especially arises in the reduced scale with low approaching velocity.

The reason for employing scaled-down experiments or simulations to study indoor airflow in natural ventilation under nonisothermal conditions is evident. Despite the significance of Re and Ar similarity requirements, there is a lack of empirical evidence concerning the impact

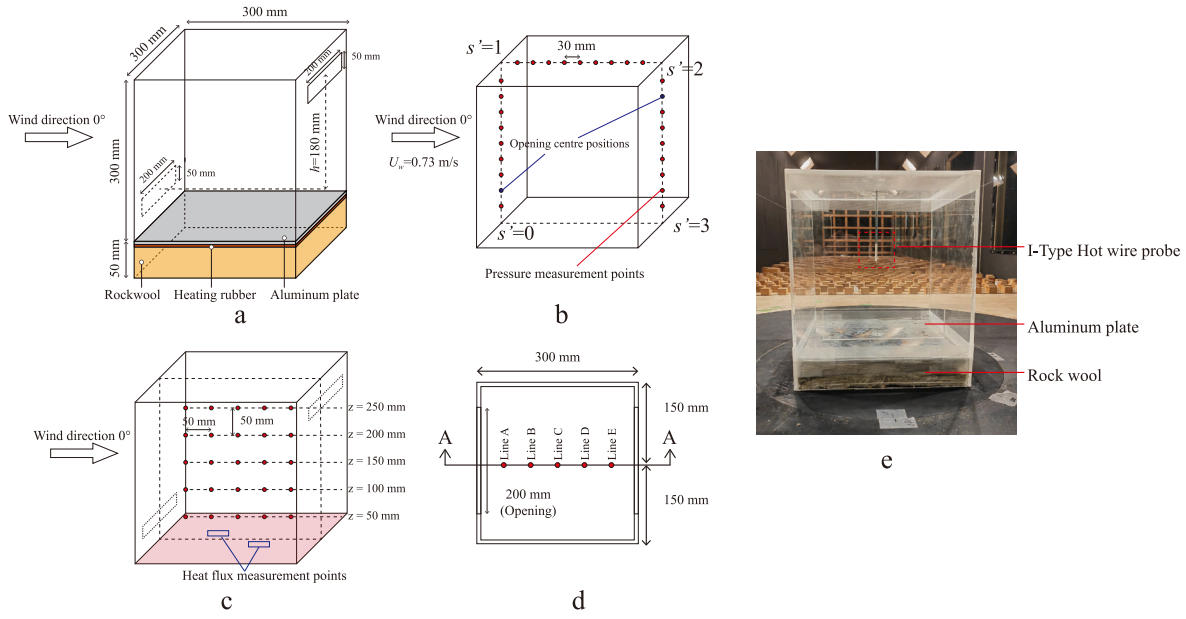

Fig. 2. (a) Building dimension. (b) Pressure measurement points. (c) Measurement points for velocity and air temperature. (d) Floor plan of the model and position of Section A. (e) Photo of velocity measurement.

of Re under nonisothermal conditions. Therefore, the primary aim of the current research was to investigate the effects of Re and *Ar* on indoor airflow patterns and ventilation rates within a reduced-scale model compared to a full-scale model using numerical analysis. A wind tunnel experiment was first conducted to validate the CFD accuracy. Subsequently, the indoor airflow and ventilation rate in the 1:10 reduced-scale model were compared with those in the full-scale model.

The wind tunnel experiment for validation of the data measurement and building geometry is reported in Section 2. Section 3 introduces the numerical settings, grid independence analysis, and the impact of the turbulence models. Section 4 presents the simulation cases for the parametric study and the similarity evaluation index. Section 5 compares the flow regimes under isothermal and nonisothermal conditions. Finally, Section 6 concludes the paper and discusses its limitations and prospects.

2. Wind tunnel experiment for validation data

A wind tunnel experiment was performed to measure the boundary layer profiles for the boundary conditions and to obtain validation data for the numerical simulations of the reduced-scale model.

2.1. Atmospheric boundary layer profile

The experimental setup of the wind tunnel is shown in Fig. 1(a). The wind tunnel is located at Osaka University, Japan, and it has a test section of 9.5 $(L) \times 1.8\ (W) \times 1.6\ m\ (H)$ [24,25,61]. The movable guide vanes at the corner located downstream of the test section make it possible to switch the type of wind tunnel between open and closed circuits. An open circuit was used for subsequent measurements.

The atmospheric boundary layer was created by combining a turbulence lattice and wooden roughness blocks. Vertical profiles of mean wind velocity and turbulence intensity were measured using an I-type hot-wire probe (0251R-T5, Kanomax) with a constant-temperature anemometer unit. The experiment included isothermal and nonisothermal measurements and a three-dimensional (3D) ultrasonic anemometer probe (TR-92T) at a height of 1 m from the floor was used to monitor the approaching velocity at 1 Hz. For the nonisothermal experiments, the reference wind velocity at the building height (0.35 m) was $U_w = 0.73$ m/s and the turbulence intensity at the building height was approximately 14 %. The turbulent kinetic energy k (m^2/s^2) was calculated as follows:

$$k = \frac{3}{2}(UI)^2 \tag{9}$$

where U is the mean velocity (m) and I is the turbulence intensity (%). Because an I-type hot-wire probe measures two velocity components, k can be calculated based on the assumption that the three velocity fluctuations are of the same order, which yields the following equation:

$$k = \frac{3}{4}(UI)^2 \tag{10}$$

Turbulence dissipation rate ε (m^2/s^3) and turbulence-specific dissipation rate ω (1/s) are calculated according to the equations below:

$$\varepsilon = \frac{C_\mu^{0.75} k^{1.5}}{L} \tag{11}$$

$$\omega = \frac{k^{0.5}}{C_\mu^{0.25} L} \tag{12}$$

where C_μ is a model constant equal to 0.09, and L is the turbulent length scale (m).

For the isothermal experiment, the indoor velocity becomes extremely small and could not be accurately measured by a hot-wire probe, so U_w is deliberately increased to 4.6 m/s with the same roughness configuration.

The vertical profile of the measured atmospheric boundary layer for the nonisothermal experiments is shown in Fig. 1. The mean streamwise velocity of the approaching flow can be described by a power law with exponent [62,63]:

$$\frac{U_z}{U_w} = \left(\frac{z}{H_{ref}}\right)^{\alpha} \tag{13}$$

where U_z is the mean streamwise velocity (m/s) at height z, U_w is the mean streamwise velocity at the building height (m/s), z is the height from the floor (m), and H_{ref} is the building height (m). α is 0.19 in this experiment.

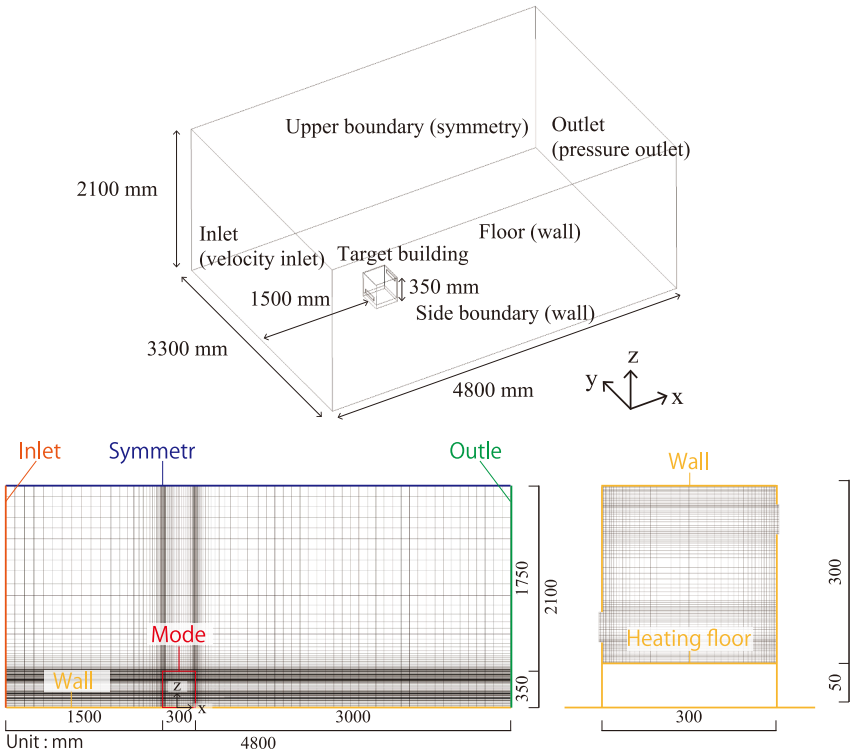

Fig. 3. Simulation domain.

2.2. The building geometry

The physical ventilation model is a 1:10 scaled-down simplified building model with dimensions of 300 × 300 × 350 mm (length × width × height), as Fig. 2(a) shows. It has two rectangular-shaped openings on the windward and leeward walls at two different heights, with a height difference between opening centres $h = 0.18$ m. The wind direction is perpendicular to the windward wall at 0°. The two same-sized openings have dimensions of 200 and 50 mm. The building model incorporates a 50 mm-thick elevated floor composed of an aluminium plate, heating rubber, and rock wool. The heating rubber, regulated by a proportional-integral-derivative (PID) temperature controller that maintains the rubber surface temperature at a given value, facilitates consistent heat generation, while the rock wool mitigates heat loss through the lower section, thereby enhancing the maximum indoor air temperature. Furthermore, an aluminium plate is employed to ensure a uniform distribution of heat across the internal floor surface. The room height above the heating floor is denoted as $H = 0.3$ m, complemented by a ceiling consisting of 5 mm-thick acrylic plates.

2.3. Validation data measurements

The validation data included pressure measurements, velocity measurements under isothermal conditions, and air temperature measurements under nonisothermal conditions. Because of the difficulty in calibrating hot-wire probes at different ambient air temperatures, the velocity and air temperature were measured separately.

Pressure measurements are important for constructing a database to predict natural ventilation rates. The surface wind pressure distribution at the centreline and the pressure difference between the positions where the two openings were located were measured using a sealed building model, as Fig. 2(b) shows. The wind tunnel is operated with $U_w = 0.73$ m/s during pressure measurement. The pressure was measured using a bell-type differential pressure gauge (ISP-320/350, Shibata) at a sampling frequency of 1000 Hz for 60 s. The wind pressure coefficient is defined as

$$Cp = \frac{p_s - p_{ref}}{\frac{1}{2}\rho U_w^2} \tag{14}$$

where p_s is the static pressure at the measurement point (Pa), p_{ref} is the reference static pressure (Pa), and U_w is the reference building height velocity (m/s) converted using the ultrasonic anemometer probe.

Fig. 2(c) shows the velocity and air temperature measurement points in the building model in Section A as illustrated in Fig. 2(d). During velocity measurement under isothermal conditions, the heating rubber was turned off. The indoor velocity was measured for 60 s at each measurement location using an I-type hot-wire probe (0251R-T5, Kanomax) with a sampling frequency of 1000 Hz, at each measurement location as Fig. 2(d) shows. There were five circular holes in the ceiling of the building model, which allowed the insertion of the hot-wire probe through one of the holes, while the rest were sealed with tape. The hot-wire probe was mounted on the mechanical arm, and the movement was controlled using in-house software with an accuracy of 0.001 mm. Simultaneously, the pressure at the reference point, situated at a height of 0.95 m from the floor within the wind tunnel, was recorded. These pressure data were utilised in deriving the mean reference building height velocity, denoted as U_w, which was approximately 4.6 m/s for isothermal experiments. The normalised velocity U/U_w was used to validate the velocity of the CFD simulation described in **Section 3.4**.

During the air temperature measurement, the heating rubber was turned on, and the wind tunnel was operated at $U_w = 0.73$ m/s. The indoor air temperature was recorded using thermocouples, whereas the heat flux on the floor was measured using two heat flux meters (Energy Eye-D0001, DENSO) with a sampling frequency of 1 Hz. Thermocouples were attached to five vertical metal poles, and the temperature was measured simultaneously. This measurement was conducted for more than 20 min after the attainment of a stable indoor air temperature was confirmed. The average values obtained from the two flux meters were

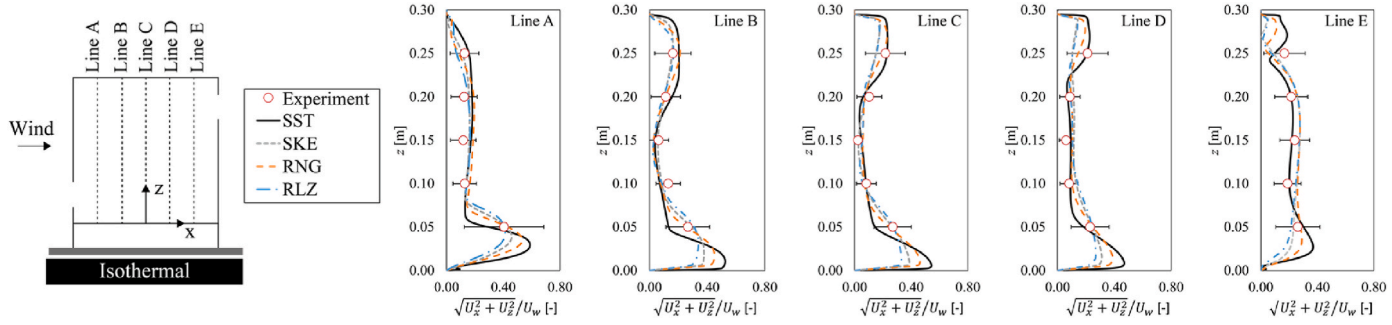

Fig. 4. Vertical profiles of mean dimensionless velocity ($\sqrt{U_x^2+U_z^2}/U_w$) at Section An under isothermal conditions using different turbulence models.

then used as the boundary conditions for the heated floor, as explained in Section 3.5.

3. CFD validation

The computational geometry, computational domain, numerical method, turbulence model, grid sensitivity analysis, and temperature validation are presented in this section.

3.1. Computation geometry, domain

The commercial CFD software ANSYS Fluent 2023 R1 was used for the steady Reynolds-averaged Navier–Stokes (RANS) computations based on the finite volume method. The building geometry was identical to that of the physical building model used in the wind tunnel experiments. The boundary conditions were set according to the guidelines provided by Tominaga et al. [64] as Fig. 3 shows. The reduced-scale computational domain had dimensions of 4800 (x) × 3300 (y) × 2100 mm (z), and the distance between the inlet boundary and the windward face of the building model was 1500 mm. The computational domain of the full-scale model was scaled up by a factor of 10. Vertical profiles of the inlet boundary were obtained based on the measurement data from the wind tunnel experiment described in Section 2.1.

3.2. Numerical methods

Pressure–velocity coupling is facilitated through the implementation of a coupled scheme based on a pressure-based coupled algorithm [65]. The Green–Gauss cell-based scheme was applied for the gradient discretisation. A higher-order differencing scheme, Quadratic Upstream Interpolation for Convective Kinematics (QUICK) was applied to discretise the advection terms [66]. Enhanced thermal wall functions based on the Kader blending method [67] were applied to the near-wall treatment of the energy equations. The selection of the computational grid resolution is explained in Section 3.4. In all equations, the residuals fell to less than 10^{-5} and converged well.

3.3. Validation metrics

The following validation metrics were used to quantify the agreement between the CFD prediction and experimental results [68]: root mean square error (RMSE), mean normalised gross error (MNGE), the fraction within a factor of two (FAC2) of the predicted observations, and normalised mean square error (NMSE). These metrics are defined as follows.

$$RMSE = \sqrt{\frac{1}{N}\sum_{i=1}^{N}(P_i - O_i)^2} \quad (15)$$

Table 1
Validation metrics for the dimensionless velocity $\sqrt{U_x^2+U_z^2}/U_w$.

	Standard k-ε	RNG k-ε	Realizable k-ε	SST k-ω
RMSE	0.10	0.07	0.07	0.05
MNGE	0.46	0.54	0.48	0.29
FAC2	0.84	0.76	0.80	0.96
NMSE	0.37	0.19	0.17	0.12

$$MNGE = \frac{1}{N}\sum_{i=1}^{N}\left|\frac{P_i - O_i}{O_i}\right| (16.) \quad (16)$$

$$FAC2 = \frac{1}{N}\sum_{i=1}^{N} n_i \text{ with } n_i = \begin{cases} 1, if\ 0.5 \le \dfrac{P_i}{O_i} \le 2.0 \\ 0, \text{otherwise} \end{cases} (17.) \quad (17)$$

$$NMSE = \frac{\frac{1}{N}\sum_{i=1}^{N}(P_i - O_i)^2}{\left(\frac{1}{N}\sum_{i=1}^{N}P_i\right)\left(\frac{1}{N}\sum_{i=1}^{N}O_i\right)} (18.) \quad (18)$$

where O_i and P_i are the measured and predicted values of a given variable for sample i, respectively, and N is the number of data points. The ideal values of the metrics corresponding to perfect agreement are 1.0 FAC2 and 0 RMSE.

3.4. Turbulence model

Turbulence models play an important role in CFD simulations. Fig. 4 compares the isothermal simulation results of dimensionless velocity at five vertical lines from four turbulence models, that is, the standard k-ε (SKE) model, RNG k-ε (RNG) model, realizable k-ε (RLZ) model, and the shear stress transport (SST) k-ω model. The circle plots the measured values, and the horizontal bar shows the normalised standard deviation of the measured velocity. Because the I-type probe measures two velocity components, the combined velocity of the x- and z-directions ($\sqrt{U_x^2+U_z^2}/U_w$) from the CFD was compared to the measurements from the wind tunnel experiment, as described in Section 2.3. The most evident difference between the simulation results of the different turbulence models can be observed in the inlet jet profile (the height of the windward opening) and the recirculation flow region at the ceiling.

Table 1 summarises the different validation metrics used to evaluate the velocity prediction accuracies of the four turbulence models. The SST k-ω model provides the best agreement with the experimentally measured velocity. Therefore, the SST k-ω model is used in the rest of the study.

In addition, the treatment of low-Reynolds-number flow also justifies

Table 2
Grid sensitivity analysis.

Grid	Number of cells	Area-weighted average $y+$ of internal surfaces
Coarse	1,287,600	2.65
Basic	2,191,600	1.54
Fine	3,716,400	0.97

the use of the SST k-ω model. Because the SKE model is developed based on the fully turbulent flow, it is inadequate for the low-Reynolds-number flow close to the wall where the viscous effect is significant. A low Reynolds k-ε model was proposed to introduce a damping function to estimate the turbulence viscosity [69]; however, it requires a very fine mesh close to the wall, which increases the computation cost. The SST k-ω model blends the k-ω model in the near-wall region and the SKE model away from the wall [70]. The combination improves the simulation accuracy in the low Reynolds region while avoiding the strong freestream sensitivity problem that the common k-ω model has [70]. Moreover, the Enhanced Wall Treatment (EWT) applied in k-ω models is independent of the y + value, which avoids significantly changing the number of meshes in reduced-scale and full-scale simulations.

The transport equations of turbulent kinetic energy (k) and specific dissipation rate (ω) are as follows [71]:

$$\frac{\partial(\rho k)}{\partial t}+\frac{\partial(\rho u_j k)}{\partial x_j}=P_k-\beta^*\rho k\omega+\frac{\partial}{\partial x_j}\left[(\mu+\sigma_k\mu_t)\frac{\partial k}{\partial x_j}\right] \tag{19}$$

$$\frac{\partial(\rho\omega)}{\partial t}+\frac{\partial(\rho u_j\omega)}{\partial x_j}=\frac{\gamma}{\upsilon_t}P_k-\beta\rho\omega^2+\frac{\partial}{\partial x_j}\left[(\mu+\sigma_\omega\mu_t)\frac{\partial\omega}{\partial x_j}\right]+2(1-F_1)\frac{\beta\sigma_{\omega2}}{\omega}\frac{\partial k}{\partial x_j}\frac{\partial\omega}{\partial x_j} \tag{20}$$

where

$$P_k=min\left[\tau_{ij}\frac{\partial u_i}{\partial x_j},10\beta^*k\omega\right] \tag{21}$$

The eddy-viscosity is obtained by

$$\mu_t=\frac{\rho k}{\omega}\frac{1}{max\left[\frac{1}{\alpha^*},\frac{SF_2}{a_1\omega}\right]} \tag{22}$$

S is the strain rate magnitude and F_2 is given by

$$F_2=tan\,h\left(\phi_2^2\right) \tag{23}$$

$$\phi_2=\max\left[2\frac{\sqrt{k}}{0.09\omega y},\frac{500\mu}{\rho y^2\omega}\right] \tag{24}$$

The coefficient α^* damps the turbulent viscosity causing a low-Reynolds-number correction:

$$\alpha^*=\alpha_\infty^*\left(\frac{\alpha_0^*+Re_t/R_k}{1+Re_t/R_k}\right) \tag{25}$$

$$Re_t=\frac{\rho k}{\mu\omega} \tag{26}$$

$$R_k=6 \tag{27}$$

$$\alpha_0^*=\frac{\beta_i}{3} \tag{28}$$

$$\beta_i=0.072 \tag{29}$$

3.5. Grid sensitivity analysis

To investigate the grid sensitivity, the computational domain was discretised using three grid sizes. Simulations were performed for each grid configuration under isothermal conditions. The total number of cells and area-weighted average y^+ of the building interior surfaces are summarised in Table 2. The coarse grid contained 1,287,600 cells with $y+=2.65$, whereas the very fine grid contained 3,716,400 cells with $y^+=0.97$. The SST k-ω model was adopted as the turbulence model. Fig. 5 compares the results of the dimensionless scalar velocity (U/U_w) for the three grids. In addition to the discrepancy in the coarse grid, a minor deviation was observed between the basic and fine grids. Therefore, a basic grid system was adopted for the remaining cases. Because the EWT was applied for all k-ω models in ANSYS Fluent, EWT is y + insensitive, which ensures it can work with high and low values of y + [71].

3.6. Temperature validation under nonisothermal simulation

The Boussinesq approximation, which treats the fluid density as a constant value, is a common approach used in isothermal simulations [72]. However, the approximation is only accurate when the density difference is small ($\Delta\rho/\rho\ll1$) [73], so it may lose applicability when the air density difference is significant [74]. Therefore, for nonisothermal simulation in the present study, the air density is interpolated by a polynomial profile between air temperature of 0 °C and 100 °C. The surface-to-surface (S2S) radiation model was used for indoor radiation exchange calculations [71], and the internal emissivity of all internal surfaces was set to 0.9. Radiation, conductance, and convection were considered for temperature validation. The inlet air temperature was set at 19.5 °C, which was the air temperature of the approaching flow measured in the wind tunnel experiment. The heat fluxes from the floor were uniformly assigned the same values as those obtained from the experimental results (2196 W/m^2). The thermal and physical properties of the acrylic materials were applied to the walls to determine heat conductance through the internal wall. The convective heat transfer coefficient was estimated to be 3.42 $W/(m^2\bullet K)$ for internal walls.

Fig. 6 plots the experiment measurements of CFD simulation results of temperature distributions at the vertical plane. Notably, the

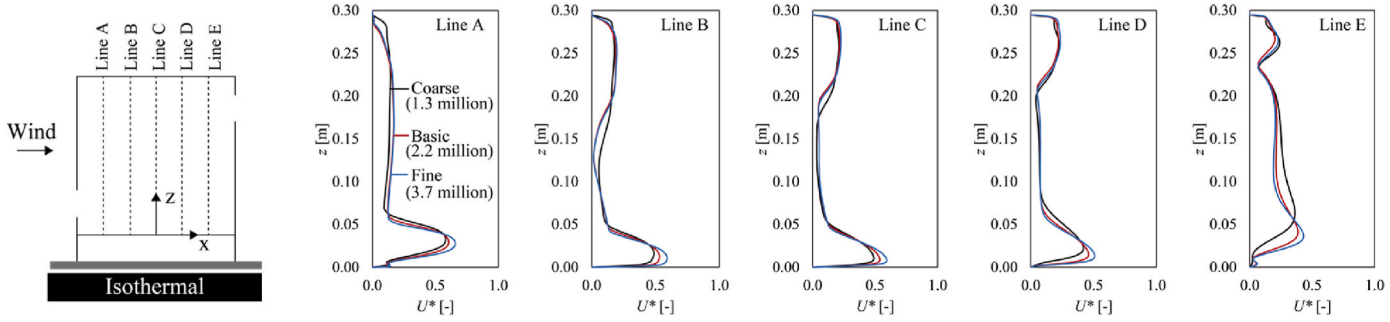

Fig. 5. Grid-sensitivity analysis results.

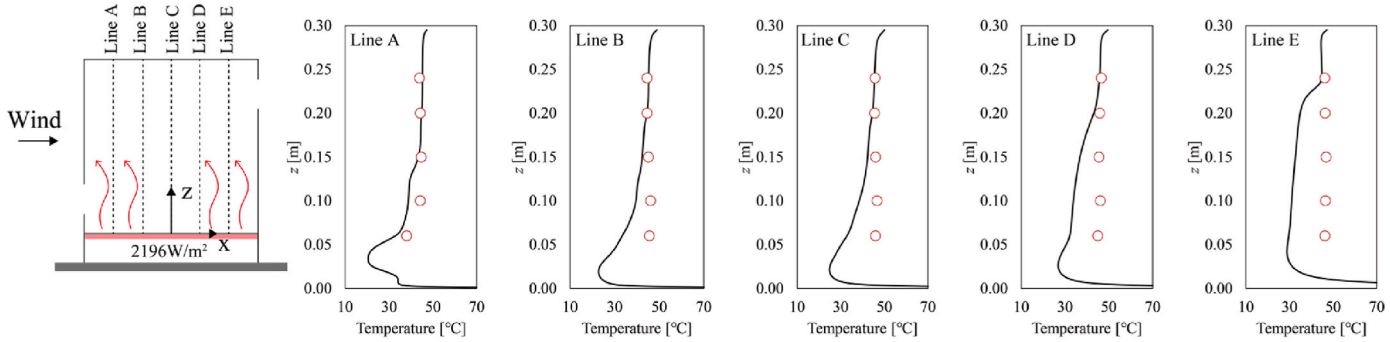

Fig. 6. Vertical profiles of temperature at Section An under nonisothermal conditions.

Table 3
Validation metrics for the temperature.

Validation index	RMSE	MNGE	FAC2	NMSE
Value	9.58	0.16	1.0	0.05

Table 4
Summary of simulated cases.

Case	Scale	U_w (m/s)	ΔT (K)	Ar	Re_o
1	Full-scale	1.46	0	0	28,867
2	1:10	0.73	0	0	1498
3	Reduced-scale	0.58			1206
4		0.44			914
5		0.29			618
6		0.15			318
7		0.07			164
8	Full-scale	1.46	10	0.29	38,719
9	1:10	0.73	25	0.29	1976
10	Reduced-scale	0.58	16		1587
11		0.44	9		1199
12		0.29	4		811
13		0.15	1		419
14		0.07	0.28		216
15	Full-scale	1.46	20	0.58	46,151
16	1:10	0.73	50	0.58	2348
17	Reduced-scale	0.58	32		1896
18		0.44	18		1436
19		0.29	8		970
20		0.15	2		499
21		0.07	0.5		256

temperature exhibits a relatively uniform distribution within the building model. Table 3 lists the validation metrics for nonisothermal simulations by comparing CFD results and experiment measurements.

Certain factors contributed to the disparities between the experimental and simulated outcomes. In the experimental setup, spatial variations in the heat flux of the heating rubber persisted. For example, the heat flux at the front heat flux meter was 3140 W/m^2 and the heat flux at the back heat flux meter was 1409 W/m^2, but only the average heat flux values were uniformly used for the indoor floor in the simulation. Additionally, the attachment of thermocouples to the aluminium poles introduced potential influences on the measurement results. Furthermore, within the simulation, uniform heat transfer coefficient values were assigned to all internal wall surfaces, potentially leading to an underestimation of the temperatures in proximity to the leeward wall in the simulation, such as along lines D and E in Fig. 6.

4. Parametric studies in CFD

4.1. Case descriptions

In the present study, simulations were conducted at both the full-scale and 1:10 reduced-scale, with Ar computed using Equation (6). The flow patterns of the reduced-scale and full-scale models were compared. Herein, ΔT is the temperature difference between indoor volume-averaged air temperature and outdoor air temperature (K), U is the building height wind velocity in the approaching flow (U_w, m/s), and L is the height difference between the centres of two openings (h, m). Table 4 summarises the building height velocity (U_w) and temperature difference ΔT in the present study with the corresponding Reynolds number at the opening scale, which results in a total of 21 simulation cases. To show the typical natural ventilation condition, in Case Ar = 0.29, the inlet air temperature (ambient air temperature) is specified as 10 °C and the indoor average air temperature in full-scale is 20 °C, which are autumn season conditions. In Case Ar = 0.58, the inlet air temperature is set to 0 °C, and the indoor average air temperature is 20 °C, which are winter season conditions.

An adiabatic thermal boundary condition was applied in the simulations of the parametric study cases. Uniform assignment of heat fluxes from the floor was implemented, and a proportional control method was employed to regulate the floor temperature according to the required indoor volume-averaged air temperature, thereby achieving the desired temperature difference (ΔT).

In addition, CFD simulations for the sealed model under different approaching wind velocity profiles were performed to confirm the influence of the Reynolds number on the wind pressure coefficient distribution at the building scale. The results are discussed in Section 5.3.

4.2. Similarity evaluation

In previous studies, several indices, such as the Deviation Rate [41,45,75], Ratio of Relative Changes [40], Adapted Deviation Rate [38], and revised Relative Change Ratio [39], were proposed to quantitatively evaluate the similarity among flow fields with different Re numbers.

The Deviation Rate (DR) of Cui et al. [41] was defined as

$$DR = \left| \frac{U^*_{Rei} - U^*_{Rej}}{U^*_{Rej}} \right| \tag{30}$$

where U^*_{Rei} and U^*_{Rej} represent the mean dimensionless velocities corresponding to two consecutive Reynolds numbers, *Rei* and *Rej*, respectively. Nevertheless, in areas characterised by lower velocities, even a slight disparity in the dimensionless velocity can lead to a significant change in *DR*. Furthermore, this approach evaluates the flow field with adjacent Re numbers, which makes it difficult to compare all cases using the same criteria.

In this study, the Mean Error (*ME*) [76] was used to evaluate similarity, which is defined as follows:

$$ME = \frac{1}{N} \sum_{i=1}^{N} \left| U^*_{reduced-scale,i} - U^*_{full-scale} \right| \tag{31}$$

where $U^*_{reduced-scale,i}$ and $U^*_{full-scale}$ represent the dimensionless velocities

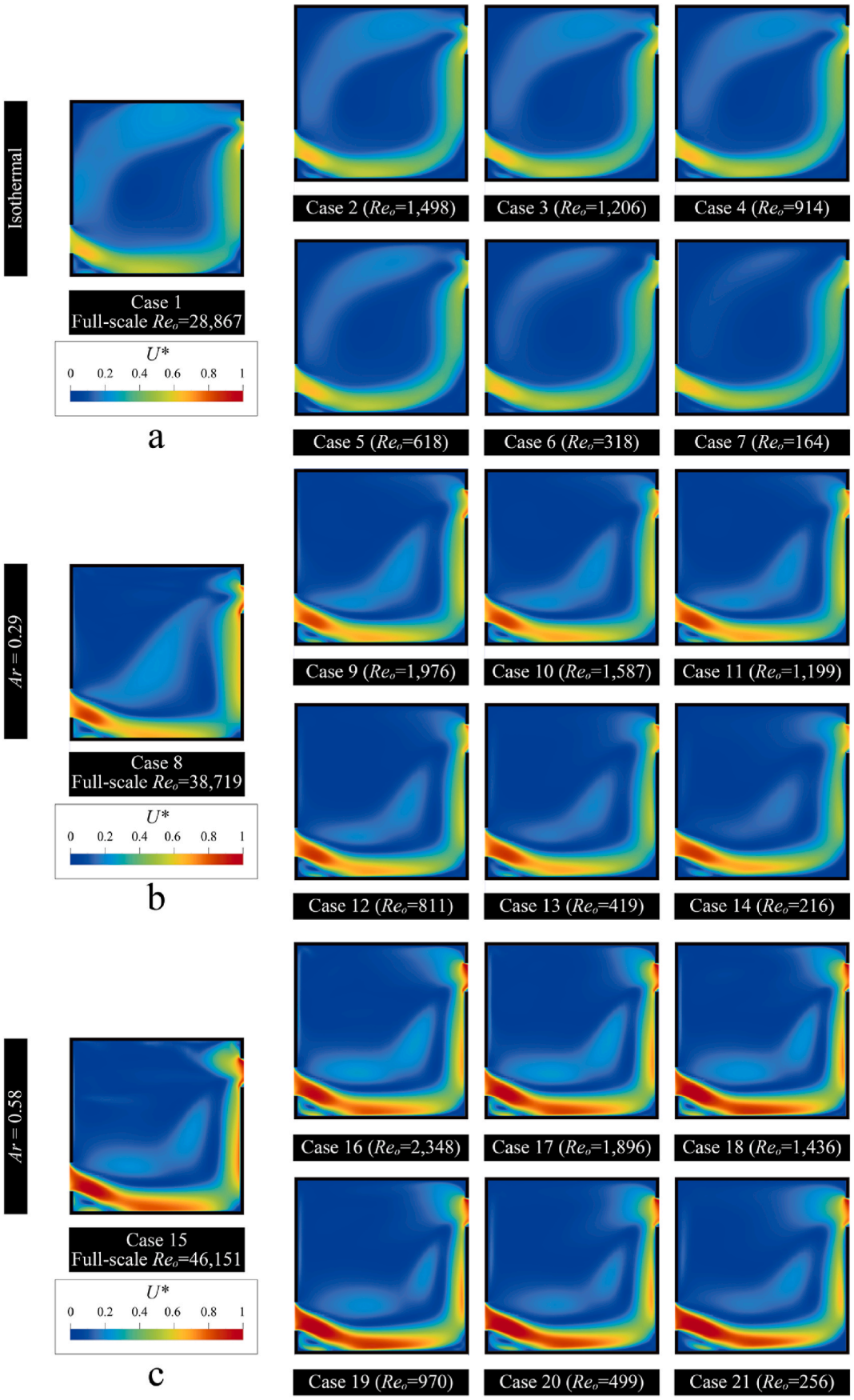

Fig. 7. Contours of the dimensionless velocity U^* at Section A: (a) isothermal conditions. (b) Ar = 0.29. (c) Ar = 0.58.

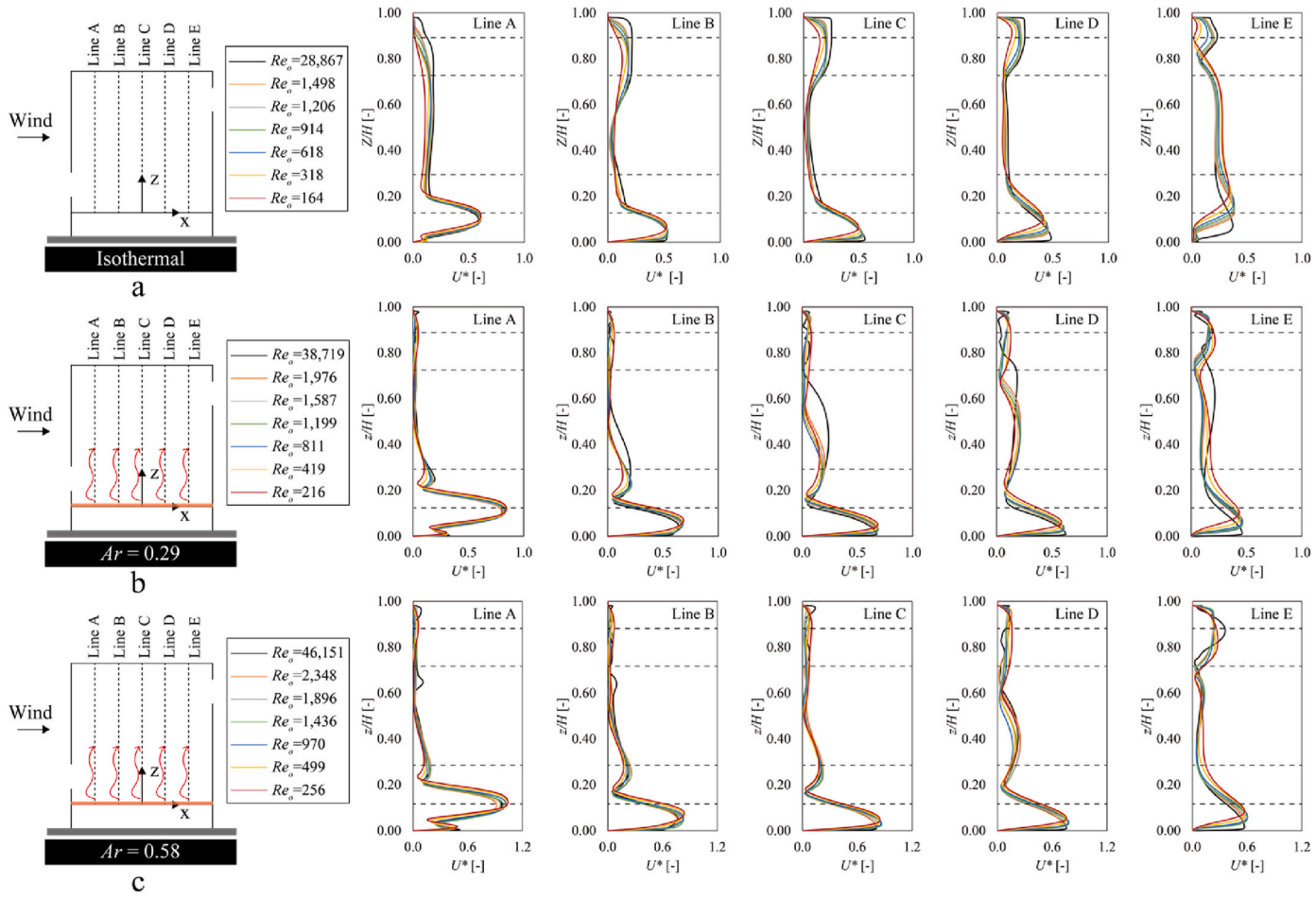

Fig. 8. Vertical profile of U^* at Section A: (a) isothermal conditions. (b) $Ar = 0.29$. (c) $Ar = 0.58$. The dashed line shows the height of the opening positions.

in the reduced- and full-scale simulations, respectively. The average error at each node along the five measurement lines was used to evaluate the similarity quantitatively. The *ME* of dimensionless temperature T^* and dimensionless ventilation rate Q^* were calculated in the same manner. T^* is defined as

$$T^* = \frac{T_i - T_{out}}{T_{in} - T_{out}}, \tag{32}$$

where T_i is the local air temperature, T_{out} is the outdoor air temperature, and T_{in} is the average indoor air temperature.

5. Simulation results of parametric studies

5.1. Velocity field

The velocity contours under isothermal and nonisothermal conditions are shown in Fig. 7. The primary ventilation flow pathway was similar under both isothermal and nonisothermal conditions: the inflow entered through the windward lower opening, adhered to the floor, ascended along the leeward wall, and exited through the leeward upper opening. At an equivalent wind force magnitude, a higher *Ar* signifies a greater buoyancy strength, resulting in a higher inflow velocity for conditions characterised by high *Ar*.

Under isothermal conditions, a secondary recirculation zone is observed, whereas, in a flow field with a lower Re_o, the recirculating flow is weakened. This weakening is attributed to the transition from a turbulent flow to a more laminar flow, where the viscous forces dominate the inertial forces.

Under nonisothermal conditions, the recirculation flow was largely altered. The accumulation of warm air at the top of the room hinders the recirculation of cold air, which is characterised by a higher density, in a manner different from that observed under isothermal conditions. Similar to the isothermal conditions, the recirculation flow also diminished in scenarios with a lower Re_o.

Fig. 8 shows a comparison of the dimensionless velocity U^* distribution under various conditions for the isothermal and nonisothermal simulations. Under isothermal conditions, notable disparities were observed, particularly in the upper region of the room where the recirculating flow is prominent and in the lower section along Line E, close to the leeward wall, which aligns with the findings reported in earlier studies [77]. In instances of low Re_o, the incoming air tends to ascend more rapidly, coupled with a reduction in the speed of the recirculating flow. A comparative analysis of the flow fields with varying *Ar* reveals that stronger buoyancy forces impede the recirculating flow at the upper section of the room while concurrently accelerating the outflow near the leeward upper opening (upper part on Line E).

An important term that determines the indoor flow pattern is the dimensionless turbulent viscosity [38]; to compare the turbulent viscosity under different approaching flow and varying building scale conditions, the dimensionless kinematic turbulent viscosity (v_t^*) is defined as follows:

$$v_t^* = \frac{\mu_t}{\rho u_o L}$$

where μ_t is the turbulent viscosity (or eddy viscosity), ρ is the air density, u_o is mean velocity, and L is the hydraulic diameter of the openings. Fig. 9 compares the v_t^* distribution under different Reynolds number conditions. The most significant differences were observed between the

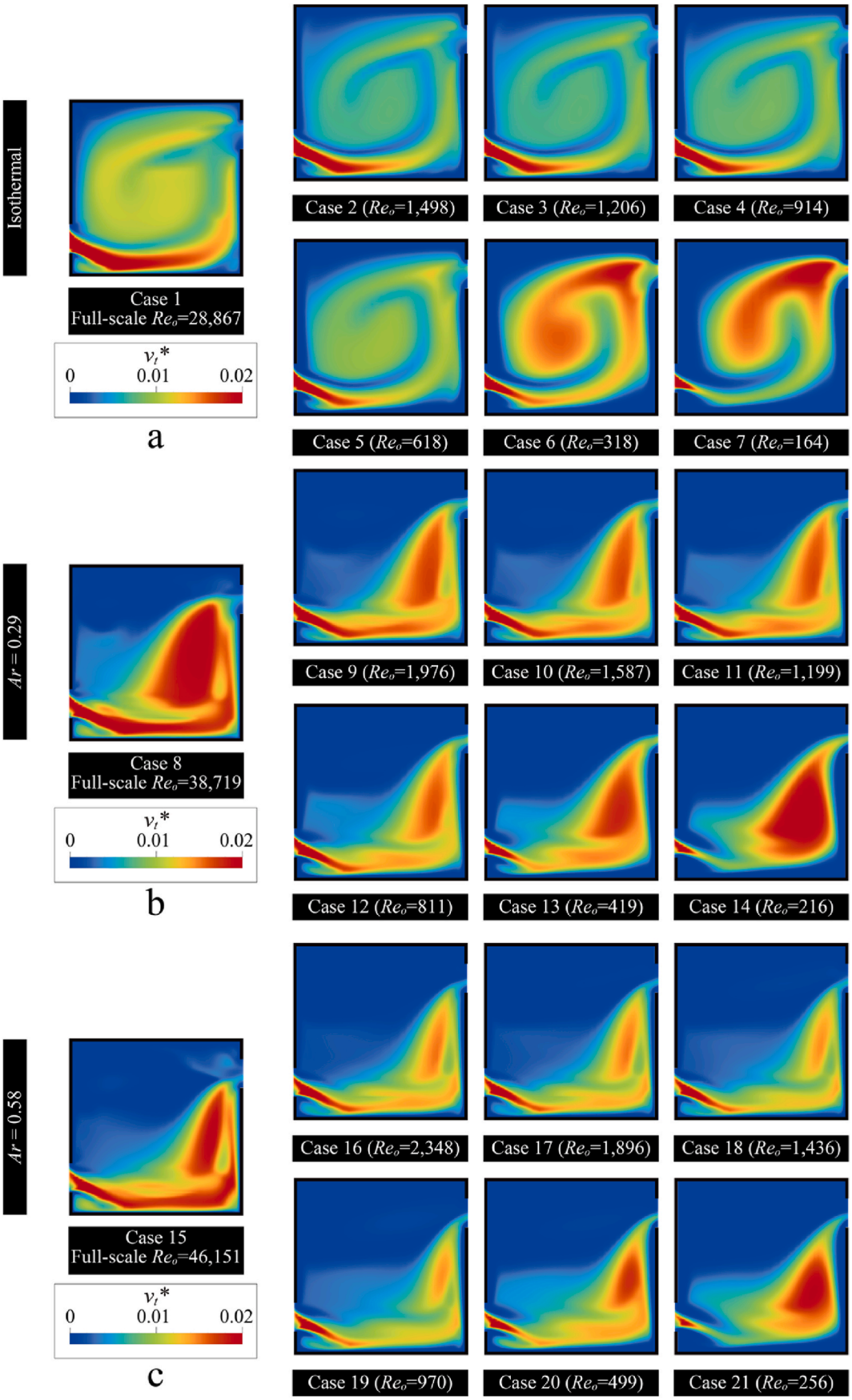

Fig. 9. Contours of the dimensionless kinematic turbulent viscosity v_t^* at Section A:
(a) isothermal conditions. (b) $Ar = 0.29$. (c) $Ar = 0.58$.

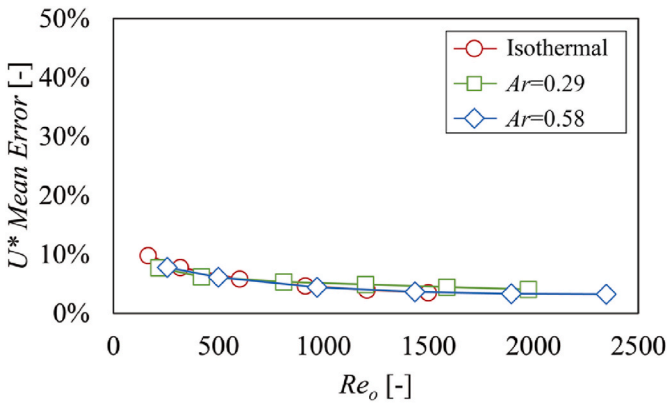

Fig. 10. *U* Mean Error* in different cases for reduced-scale simulation compared to full-scale simulation.

inflow and recirculation flows. In comparison to the full-scale scenario, v_t^* diminishes within the inflow region and increases within the recirculation region as the Re_o decreases. In indoor airflow characterised by a lower Re_o, it can be anticipated that the diffusion will be less pronounced compared to cases with a higher Re_o, which results in a difference in U^* on the lower part of Line E and the recirculation region.

Fig. 10 plots the U^* deviation rate in each flow field characterized by varying Re_o. The deviation rate trends remain largely consistent across different *Ar* scenarios, exhibiting a decline as the Re_o increases. In isothermal conditions, the maximum deviation rate of 10 % is evident at $Re_o = 164$, whereas deviations are consistently below 5 % for Re_o surpassing 1000.

5.2. Temperature field

Fig. 11 illustrates the T^* contours in the nonisothermal simulation. The warm air ascends and ultimately gathers in the upper zone of the room, whereas cold air enters through the windward lower opening to ventilate and cool the indoor environment, particularly along the ventilation pathway. Notably, an observable discrepancy between the various Reynolds numbers Re_o was only discernible in the upper region of the room, where T^* was higher in the flow field with a high Re_o.

Fig. 12 shows a comparison of the dimensionless temperature T^* distribution under various conditions for the nonisothermal simulations. The accumulation of warm air was evident between the leeward upper opening and the top ceiling, whereas cold air with $T^* = 0$ was confined to the area near the windward lower opening. The vertical distribution of T^* demonstrated an approximately linear trend between the heights of the two openings. Notably, this pattern cannot be accurately predicted by either the well-mixed model or the two-layer stratification model, which is consistent with the findings reported by Chew [78].

T^* remained relatively consistent at the height between the two openings regardless of Re_o. The most notable discrepancy occurred in the proximity of the near-wall region of the top ceiling, which was a zone minimally affected by the primary ventilation flow path. It should be noted that the similarity of radiation at different scales was not met, which partly contributed to this discrepancy. Fig. 13(a) and Fig. 13(b) illustrate the average deviation rate of T^* across all lines and at various heights between the two openings. Across all heights, the deviation rate of T^* decreased as Re_o increased, with an average deviation rate ranging from 21 % ($Re_o = 2345$) to 39 % ($Re_o = 216$). However, the T^* deviation rate within the ventilation pathway demonstrated less sensitivity to Re_o, with average deviation rates of 10 % and 6 % for all cases $Ar = 0.29$ and $Ar = 0.58$, respectively)."

5.3. Wind pressure coefficient and ventilation rate

The measured and simulated wind pressure coefficient distributions at the centreline of the sealed model are plotted in Fig. 14(a), where the bar indicates the standard deviation of the wind pressure coefficient. The simulation results agreed well with the measured wind pressure coefficient results from the wind tunnel, and the wind pressure coefficient was insensitive to Reynolds numbers as low as $Re_H = 1747$. Fig. 14 (b) plots the wind pressure coefficient difference against Re_H, and the ΔCp ranges from 0.90 to 0.92, which is also hardly influenced by Re_H.

Fig. 15(a) plots the Q^* versus Re_o. Because the wind force is the same for all cases, a higher *Ar* indicates stronger buoyancy, which contributes to a higher ventilation rate. Q^* tends to decrease when the Re_o increases in all cases; considering the ΔCp is nearly constant, it can be assumed that the dependence of Q^* on the Reynolds number is mainly caused by the discharge coefficient.

Fig. 15(b) shows the variation in the deviation rate of Q^* for different cases. A lower Re_o corresponds to an elevated deviation rate, with the most pronounced instance observed in the scenario characterized by $U_w = 0.07$ m/s and $Ar = 0.58$, yielding an opening Reynolds number $Re_o = 256$. This suggests that employing the ventilation rate determined in such a scenario to predict the full-scale ventilation rate results in an error of approximately 9 %.

Based on the ventilation rate simulation results in the present study, if Re_o at the reduced scale is larger than 1,000, the full-scale ventilation rate can be directly extrapolated with an error of less than 5 %. However, a Re_o lower than 1000 may cause an error of as much as 9 %. The findings are close to the previous conclusions made by Etheridge and Nolan [79], that it is reasonable to assume Q^* has a constant value for $U_o\sqrt{A}/\upsilon > 2,000$ [36].

The error in the dimensionless ventilation rate prediction at a low Re flow can be diminished by using a corrected C_d based on Re_o. Many previous studies have attempted to propose an empirical model to predict the discharge coefficient at a low Re number for orifice flow. The model proposed by Wu et al. [80] was used to correct the discharge coefficient:

$$f(Re_o) = C_{d\infty}\left(1 + ae^{-\frac{\delta_1}{C_{d\infty}}\sqrt{Re}} + be^{-\frac{\delta_2}{C_{d\infty}}\sqrt{Re}}\right) \tag{33}$$

where the parameters, a, b, δ_1, and δ_2 are specific flow-dependent coefficients that should be determined. Here, $C_{d\infty}$ is set to be 0.6, which is commonly used for natural ventilation rate prediction [36] and $a = 1.07$, $b = -2.07$, $\delta_1 = 0.077$, and $\delta_1 = 0.15$, which are determined by Merritt's data [81]. With the corrected discharge coefficient, Q^* can be predicted as follows:

$$Q^* = f(Re_o)\sqrt{\Delta Cp + 2Ar} \tag{34}$$

Fig. 15(a) compares the ventilation rate predicted by the corrected C_d and constant $C_d = 0.6$. The prediction of Q^* with corrected C_d had a mean error of 3 % compared to the simulated ventilation rate. It should be emphasised that the empirical discharge coefficient correction equation was based on general orifice plates that were not specially designed for natural ventilation problems. Therefore, it is only used as an alternative method to consider the low-Reynolds-number effect, instead of using this specific equation for ventilation rate prediction.

6. Conclusion

The similarity criterion is vitally important in reduced-scale experiments and simulations. In this study, the Re and *Ar* similarities for reduced-scale simulations under isothermal and nonisothermal conditions were investigated using a series of RANS simulations with the same *Ar* but varying velocity and temperature combinations. The main findings are summarised below.

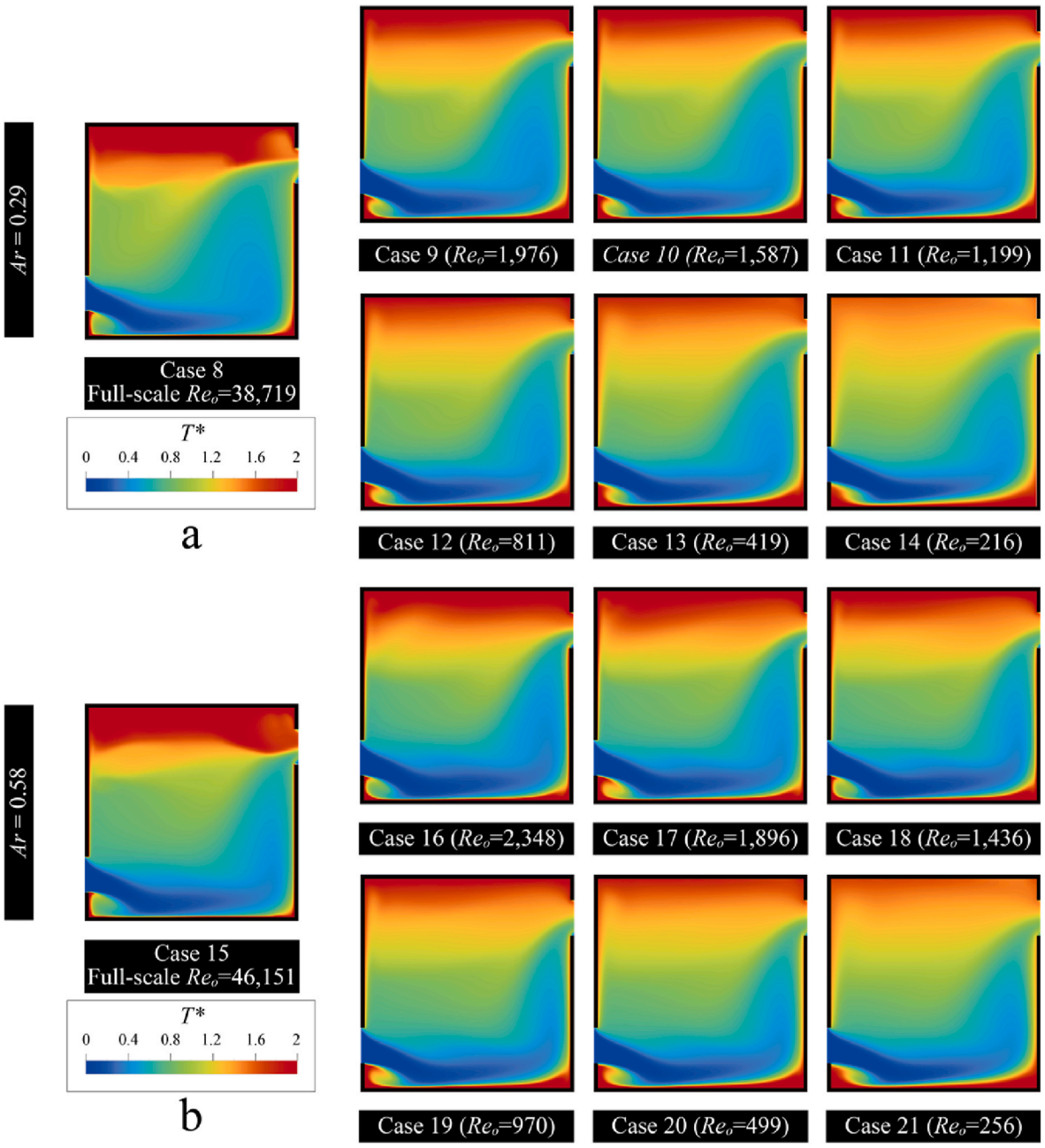

Fig. 11. Contours of the dimensionless temperature T^* at Section A:
(a) $Ar = 0.29$, (b) $Ar = 0.58$.

The CFD simulation results of the velocity agreed well with the measured values from the experiment under isothermal conditions, but the temperature of the simulation deviated from the measured values. This results from several assumed coefficients, such as the heat transfer coefficient, radiation ratio, and heat conductance properties. In the studied cases, the simulations designated the internal building walls as adiabatic and neglected the thermal mass influence of the building envelope. However, the building envelope is a pivotal factor that affects the indoor environment and airflow dynamics. A more realistic flow field or simulation can be achieved by further exploring thermal mass treatments in a reduced-scale model.

Under nonisothermal conditions, *Ar* is of primary importance, although it may lead to a lower Re in the reduced-scale model. With the same *Ar*, the overall velocity and temperature fields showed the same distribution pattern in both reduced-scale and full-scale simulations. The Reynolds number at the opening scale was reconfirmed to characterise the indoor airflow field.

The velocity field caused by the low-Reynolds-number effect exhibited the highest deviation of 10 % when $Re_o = 164$. In the low-velocity area, the recirculating flow and near-wall region showed the greatest dependence on the Re number. This deviation can be reduced to less than 5 % if Re_o can exceed 1000.

The temperature field was more influenced by Re_o than the velocity field, whereas the most obvious discrepancy occurred at the boundary walls, where a high Re_o led to a higher temperature gradient. The overall temperature deviates by approximately 40 % when Re_o is as low as 164, whereas the deviation of the temperature field on the ventilation pathway is less than 10 %, regardless of Re_o. The thermal stratification patterns between the reduced- and full-scale models are similar and cannot be described by a well-mixed model or two-layer stratification

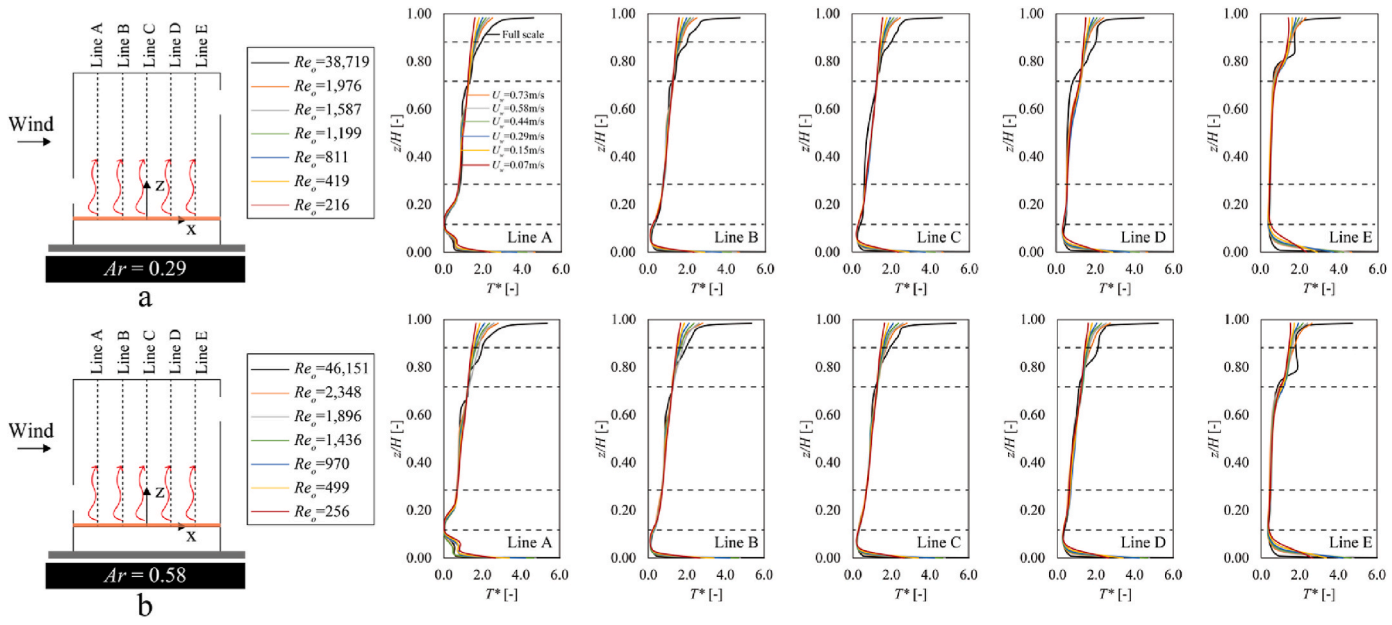

Fig. 12. Vertical profile of T^* at Section A
(a) $Ar = 0.29$. (b) $Ar = 0.58$. The dashed line shows the height of the opening positions.

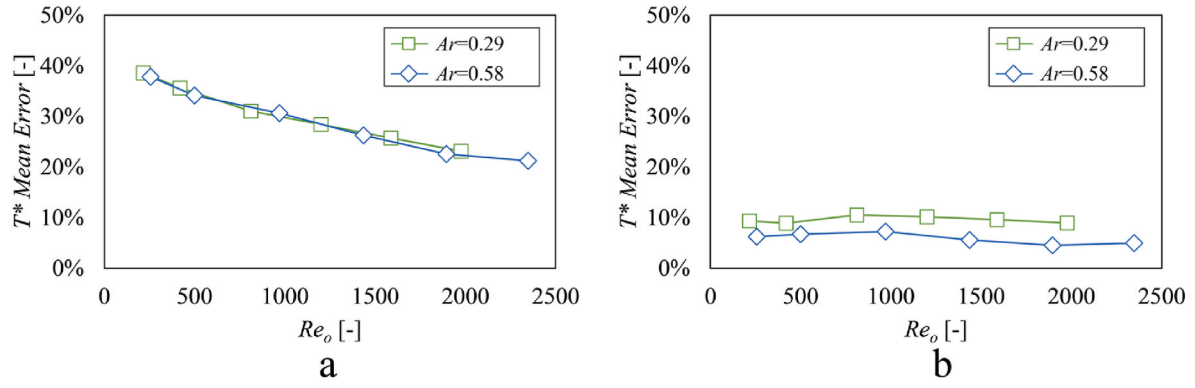

Fig. 13. *T* Mean Error* for reduced-scale simulation compared to full-scale simulation: (a) in all lines. (b) At heights between two openings.

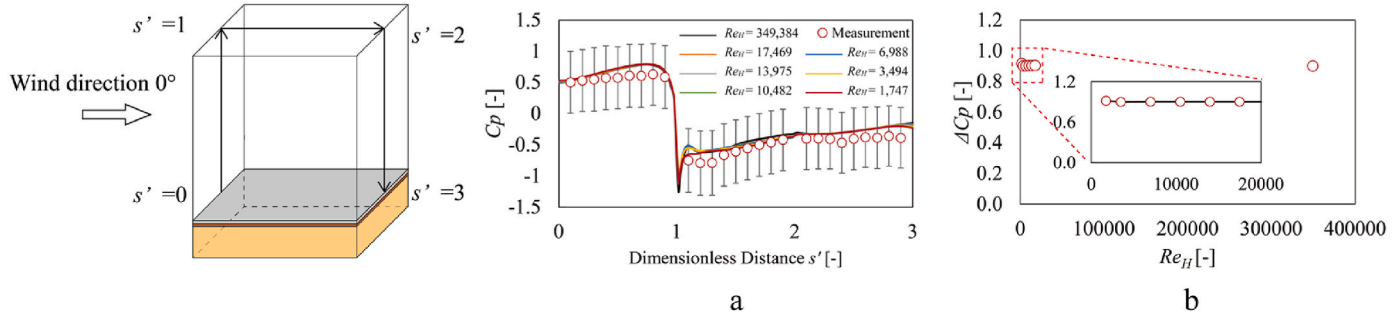

Fig. 14. (a) Pressure coefficient (*Cp*) distribution under different approaching flow conditions. (b) Pressure coefficient difference under Re_H number flow.

model.

The pressure distribution was much less sensitive to Re_H even when Re_H was as low as 1747. The dimensionless ventilation rate is higher when Re_o is lower, which is a result of the increasing discharge coefficient. The highest deviation in the dimensionless ventilation rate was approximately 9 % when Re_o was 256, and the deviation decreased to less than 5 % if Re_o was higher than 1000.

The following subjects are suggested for discussion and as potential areas for future investigation:

An identical grid system was employed across various simulation scales, resulting in variable $y+$ values for wall surfaces at different scales. For instance, the first cell on the 0.1 scale resides within the laminar region, whereas in a full-scale simulation, the same cell might be situated in the fully turbulent region. Consequently, distinct wall functions were applied to the near-wall cells, leading to disparities in the near-wall region.

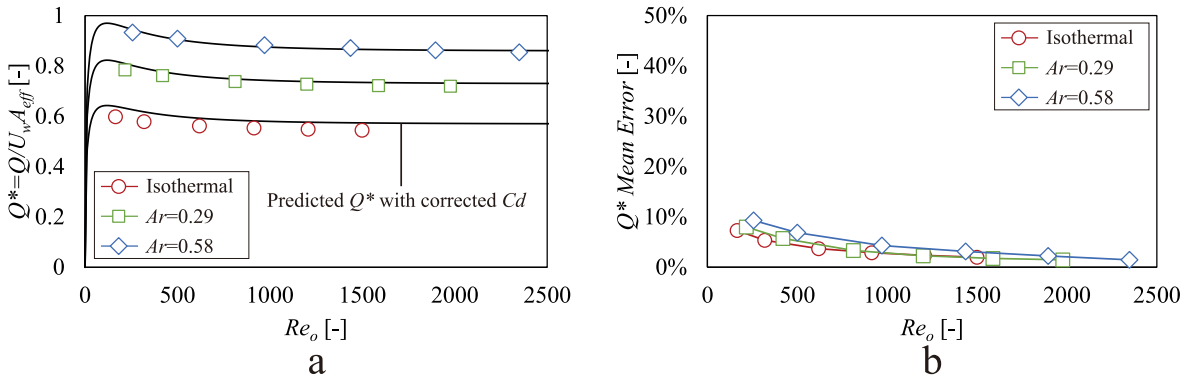

Fig. 15. (a) Dimensionless ventilation rate (Q^*) in different cases and Q^* prediction curves with corrected discharge coefficient. (b) Q^* Mean error for reduced-scale simulation compared to full-scale simulation.

The validation of nonisothermal simulations is of vital importance, but also challenging. This requires a detailed measurement of the boundary conditions and the careful selection of simulation parameters, such as the radiation model and heat transfer coefficient settings. In future studies, a more systematic parametric study of nonisothermal simulations is required to enhance the understanding of the influence of the simulation setting on the simulation results.

The investigation focused solely on buoyancy ventilation with assisting wind, resulting in a unidirectional airflow induced by either wind or buoyancy. In scenarios involving buoyancy ventilation with turbulent or opposing winds, the airflow patterns become more intricate, and the conclusions drawn from the aforementioned simulations may not be universally applicable. Future work should incorporate large eddy simulation (LES) to examine similarity issues in nonisothermal flow fields with turbulence-induced bidirectional flows.

Declaration

During the preparation of this work, the authors used GPT-3.5 developed by OpenAI, to assist in proofreading and improve language and readability. After using this tool, the authors reviewed and edited the content as needed and took responsibility for the content of the publication.

CRediT authorship contribution statement

Zitao Jiang: Writing – review & editing, Writing – original draft, Visualization, Methodology, Investigation, Formal analysis, Data curation, Conceptualization. **Tomohiro Kobayashi:** Writing – review & editing, Supervision, Resources, Project administration, Methodology, Investigation, Funding acquisition. **Toshio Yamanaka:** Resources, Investigation. **Mats Sandberg:** Investigation, Conceptualization. **Haruna Yamasawa:** Resources. **Miyazawa Shohei:** Software, Methodology, Formal analysis, Data curation.

Declaration of competing interest

The authors declare the following financial interests/personal relationships which may be considered as potential competing interests. Tomohiro Kobayashi reports financial support was provided by Japan Society for the Promotion of Science. Zitao Jiang reports financial support was provided by Japan Science and Technology Agency. If there are other authors, they declare that they have no known competing financial interests or personal relationships that could have appeared to influence the work reported in this paper.

Data availability

Data will be made available on request.

Acknowledgements

Part of this work was supported by a JSPS Grant-in-Aid for Scientific Research in Japan (Grant-in-Aid for Scientific Research(B), Grant Number: JP20H02311, Principal Investigator: Tomohiro Kobayashi) and JST SPRING, Grant Number JPMJSP2138.

References

[1] N. Cardinale, M. Micucci, F. Ruggiero, Analysis of energy saving using natural ventilation in a traditional Italian building, Energy Build. 35 (2003) 153–159, https://doi.org/10.1016/S0378-7788(02)00024-5.
[2] R.Z. Homod, K.S.M. Sahari, Energy savings by smart utilization of mechanical and natural ventilation for hybrid residential building model in passive climate, Energy Build. 60 (2013) 310–329, https://doi.org/10.1016/j.enbuild.2012.10.034.
[3] Y. Chen, L.K. Norford, H.W. Samuelson, A. Malkawi, Optimal control of HVAC and window systems for natural ventilation through reinforcement learning, Energy Build. 169 (2018) 195–205, https://doi.org/10.1016/j.enbuild.2018.03.051.
[4] Y. Chen, Z. Tong, W. Wu, H. Samuelson, A. Malkawi, L. Norford, Achieving natural ventilation potential in practice: control schemes and levels of automation, Appl. Energy 235 (2019) 1141–1152, https://doi.org/10.1016/j.apenergy.2018.11.016.
[5] B. Park, S. Lee, Investigation of the energy saving efficiency of a natural ventilation strategy in a multistory school building, Energies 13 (2020) 1746, https://doi.org/10.3390/en13071746.
[6] A.R. Escombe, C.C. Oeser, R.H. Gilman, M. Navincopa, E. Ticona, W. Pan, C. Martínez, J. Chacaltana, R. Rodríguez, D.A.J. Moore, J.S. Friedland, C.A. Evans, Natural ventilation for the prevention of airborne contagion, PLoS Med. 4 (2007) e68, https://doi.org/10.1371/journal.pmed.0040068.
[7] H.-M. Kao, T.-J. Chang, Y.-F. Hsieh, C.-H. Wang, C.-I. Hsieh, Comparison of airflow and particulate matter transport in multi-room buildings for different natural ventilation patterns, Energy Build. 41 (2009) 966–974, https://doi.org/10.1016/j.enbuild.2009.04.005.
[8] Y. Chartier, C.L. Pessoa-Silva, Natural Ventilation for Infection Control in Health-Care Settings, World Health Organization, 2009.
[9] T. Zweers, L. Preller, B. Brunekreef, J.S.M. Boleij, Health and indoor climate complaints of 7043 office workers in 61 buildings in The Netherlands, Indoor Air 2 (1992) 127–136.
[10] O. Seppanen, W.J. Fisk, Association of Ventilation System Type with SBS Symptoms in Office Workers, 2001.
[11] S.M. Dutton, D. Banks, S.L. Brunswick, W.J. Fisk, Health and economic implications of natural ventilation in California offices, Build. Environ. 67 (2013) 34–45, https://doi.org/10.1016/j.buildenv.2013.05.002.
[12] J.F. Nicol, M.A. Humphreys, Adaptive thermal comfort and sustainable thermal standards for buildings, Energy Build. 34 (2002) 563–572, https://doi.org/10.1016/S0378-7788(02)00006-3.
[13] S. Carlucci, L. Bai, R. de Dear, L. Yang, Review of adaptive thermal comfort models in built environmental regulatory documents, Build. Environ. 137 (2018) 73–89, https://doi.org/10.1016/j.buildenv.2018.03.053.
[14] R. de Dear, J. Xiong, J. Kim, B. Cao, A review of adaptive thermal comfort research since 1998, Energy Build. 214 (2020) 109893, https://doi.org/10.1016/j.enbuild.2020.109893.
[15] Z. Jiang, T. Kobayashi, T. Yamanaka, M. Sandberg, A literature review of cross ventilation in buildings, Energy Build. 291 (2023) 113143, https://doi.org/10.1016/j.enbuild.2023.113143.

[16] T. Yang, N.G. Wright, D.W. Etheridge, A.D. Quinn, A comparison of CFD and full-scale measurements for analysis of natural ventilation, Int. J. Vent. 4 (2006) 337–348, https://doi.org/10.1080/14733315.2005.11683713.
[17] T. van Hooff, B. Blocken, Full-scale measurements of indoor environmental conditions and natural ventilation in a large semi-enclosed stadium: possibilities and limitations for CFD validation, J. Wind Eng. Ind. Aerod. (2012) 104–106, https://doi.org/10.1016/j.jweia.2012.02.009, 330–341.
[18] H.L. Gough, Z. Luo, C.H. Halios, M.-F. King, C.J. Noakes, C.S.B. Grimmond, J. F. Barlow, R. Hoxey, A.D. Quinn, Field measurement of natural ventilation rate in an idealised full-scale building located in a staggered urban array: comparison between tracer gas and pressure-based methods, Build. Environ. 137 (2018) 246–256, https://doi.org/10.1016/j.buildenv.2018.03.055.
[19] S. Fan, M.S. Davies Wykes, W.E. Lin, R.L. Jones, A.G. Robins, P.F. Linden, A full-scale field study for evaluation of simple analytical models of cross ventilation and single-sided ventilation, Build. Environ. 187 (2021) 107386, https://doi.org/10.1016/j.buildenv.2020.107386.
[20] P. Karava, Airflow Prediction in Buildings for Natural Ventilation Design: Wind Tunnel Measurements and Simulation, Concordia University, 2008.
[21] T. Kobayashi, M. Sandberg, H. Kotani, L. Claesson, Experimental investigation and CFD analysis of cross-ventilated flow through single room detached house model, Build. Environ. 45 (2010) 2723–2734, https://doi.org/10.1016/j.buildenv.2010.06.001.
[22] Y. Tominaga, B. Blocken, Wind tunnel experiments on cross-ventilation flow of a generic building with contaminant dispersion in unsheltered and sheltered conditions, Build. Environ. 92 (2015) 452–461, https://doi.org/10.1016/j.buildenv.2015.05.026.
[23] H.-Y. Zhong, C. Lin, J. Shang, Y. Sun, H. Kikumoto, R. Ooka, F.-P. Qian, F.-Y. Zhao, Wind tunnel experiments on pumping ventilation through a three-story reduce-scaled building with two openings affected by upwind and downwind buildings, Build. Environ. 219 (2022) 109188, https://doi.org/10.1016/j.buildenv.2022.109188.
[24] Z. Jiang, T. Kobayashi, T. Yamanaka, M. Sandberg, N. Kobayashi, N. Choi, K. Sano, Validity of Orifice equation and impact of building parameters on wind-induced natural ventilation rates with minute mean wind pressure difference, Build. Environ. 219 (2022) 109248, https://doi.org/10.1016/j.buildenv.2022.109248.
[25] Z. Jiang, T. Kobayashi, T. Yamanaka, M. Sandberg, N. Choi, N. Kobayashi, K. Sano, K. Toyosawa, Wind tunnel experiment of wind-induced single-sided ventilation under generic sheltered urban area, Build. Environ. 242 (2023) 110615, https://doi.org/10.1016/j.buildenv.2023.110615.
[26] J.M. Holford, G.R. Hunt, Fundamental atrium design for natural ventilation, Build. Environ. 38 (2003) 409–426, https://doi.org/10.1016/S0360-1323(02)00019-7.
[27] P.-C. Liu, H.-T. Lin, J.-H. Chou, Evaluation of buoyancy-driven ventilation in atrium buildings using computational fluid dynamics and reduced-scale air model, Build. Environ. 44 (2009) 1970–1979, https://doi.org/10.1016/j.buildenv.2009.01.013.
[28] P.F. Linden, G.F. Lane-Serff, D.A. Smeed, Emptying filling boxes: the fluid mechanics of natural ventilation, J. Fluid Mech. 212 (1990) 309–335, https://doi.org/10.1017/S0022112090001987.
[29] P. Heiselberg, Y. Li, A. Andersen, Experimental and CFD evidence of multiple solutions in a naturally ventilated building, Indoor Air 14 (2004) 43–54, https://doi.org/10.1046/j.1600-0668.2003.00209.x.
[30] M.S. Davies Wykes, E. Chahour, P.F. Linden, The effect of an indoor-outdoor temperature difference on transient cross-ventilation, Build. Environ. 168 (2020) 106447, https://doi.org/10.1016/j.buildenv.2019.106447.
[31] Z.T. Ai, C.M. Mak, Potential use of reduced-scale models in CFD simulations to save numerical resources: theoretical analysis and case study of flow around an isolated building, J. Wind Eng. Ind. Aerod. 134 (2014) 25–29, https://doi.org/10.1016/j.jweia.2014.08.009.
[32] Y. Fan, Y. Zhang, S. Wang, X. Wang, J. Lu, J. Ge, A numerical rotating water tank can reproduce the Coriolis effect on the urban heat dome flow, Build. Environ. 229 (2023) 109894, https://doi.org/10.1016/j.buildenv.2022.109894.
[33] S. Wu, C. Chen, H. Song, Z. Yu, J. Wang, Y. Wang, Reduced-scale numerical simulation method and its application to urban-scale buoyancy-driven flows, Build. Environ. 249 (2024) 111117, https://doi.org/10.1016/j.buildenv.2023.111117.
[34] W.H. Snyder, Similarity criteria for the application of fluid models to the study of air pollution meteorology, Boundary-Layer Meteorol. 3 (1972) 113–134, https://doi.org/10.1007/BF00769111.
[35] W.H. Snyder, Guideline for Fluid Modeling of Atmospheric Diffusion, Environmental Sciences Research Laboratory, Office of Research and Development, U.S. Environmental Protection Agency, 1981.
[36] D.W. Etheridge, M. Sandberg, Building Ventilation: Theory and Measurement, John Wiley & Sons, Chichester, UK, 1996.
[37] Y. Dai, C.M. Mak, Z. Ai, Flow and dispersion in coupled outdoor and indoor environments: issue of Reynolds number independence, Build. Environ. 150 (2019) 119–134, https://doi.org/10.1016/j.buildenv.2019.01.008.
[38] C. Shu, L. Leon, Wang, M. Mortezazadeh, Dimensional analysis of Reynolds independence and regional critical Reynolds numbers for urban aerodynamics, J. Wind Eng. Ind. Aerod. 203 (2020) 104232, https://doi.org/10.1016/j.jweia.2020.104232.
[39] Y. Lin, J. Hang, H. Yang, L. Chen, G. Chen, H. Ling, M. Sandberg, L. Claesson, C.K. C. Lam, Investigation of the Reynolds number independence of cavity flow in 2D street canyons by wind tunnel experiments and numerical simulations, Build. Environ. 201 (2021) 107965, https://doi.org/10.1016/j.buildenv.2021.107965.
[40] P.-Y. Cui, W.-Q. Chen, J.-Q. Wang, J.-H. Zhang, Y.-D. Huang, W.-Q. Tao, Numerical studies on issues of Re-independence for indoor airflow and pollutant dispersion within an isolated building, Build. Simulat. 15 (2022) 1259–1276, https://doi.org/10.1007/s12273-021-0846-z.
[41] P.-Y. Cui, F. Yang, J.-Q. Wang, W.-Q. Chen, Y.-D. Huang, W.-Q. Tao, Numerical studies on Re-independence and influence region definition for flow and dispersion within street-indoor scale model, Build. Environ. 229 (2023) 109949, https://doi.org/10.1016/j.buildenv.2022.109949.
[42] K.C. Mehta, W.L. Coulbourne, Wind loads: guide to the wind load provisions of ASCE 7-10, American Society of Civil Engineers (2013).
[43] A.A. Townsend, The Structure of Turbulent Shear Flow, Cambridge University Press, 1956.
[44] K. Uehara, S. Wakamatsu, R. Ooka, Studies on critical Reynolds number indices for wind-tunnel experiments on flow within urban areas, Boundary-Layer Meteorol. 107 (2003) 353–370, https://doi.org/10.1023/A:1022162807729.
[45] P.-Y. Cui, Z. Li, W.-Q. Tao, Investigation of Re-independence of turbulent flow and pollutant dispersion in urban street canyon using numerical wind tunnel (NWT) models, Int. J. Heat Mass Tran. 79 (2014) 176–188, https://doi.org/10.1016/j.ijheatmasstransfer.2014.07.096.
[46] P.F. Linden, The fluid mechanics of natural ventilation, Annu. Rev. Fluid Mech. 31 (1999) 201–238, https://doi.org/10.1146/annurev.fluid.31.1.201.
[47] H.-Y. Zhong, Y. Sun, J. Shang, F.-P. Qian, F.-Y. Zhao, H. Kikumoto, C. Jimenez-Bescos, X. Liu, Single-sided natural ventilation in buildings: a critical literature review, Build. Environ. 212 (2022) 108797, https://doi.org/10.1016/j.buildenv.2022.108797.
[48] L. de O. Neves, F. Marques da Silva, Simulation and measurements of wind interference on a solar chimney performance, J. Wind Eng. Ind. Aerod. 179 (2018) 135–145, https://doi.org/10.1016/j.jweia.2018.05.020.
[49] X. Liu, X. Liu, T. Zhang, C. Lin, H.-Y. Zhong, R. Ooka, H. Kikumoto, Winter air infiltration induced by combined buoyancy and wind forces in large-space buildings, J. Wind Eng. Ind. Aerod. 210 (2021) 104501, https://doi.org/10.1016/j.jweia.2020.104501.
[50] P.-Y. Cui, Z. Li, W.-Q. Tao, Wind-tunnel measurements for thermal effects on the air flow and pollutant dispersion through different scale urban areas, Build. Environ. 97 (2016) 137–151, https://doi.org/10.1016/j.buildenv.2015.12.010.
[51] P.-Y. Cui, Z. Li, W.-Q. Tao, Buoyancy flows and pollutant dispersion through different scale urban areas: CFD simulations and wind-tunnel measurements, Build. Environ. 104 (2016) 76–91, https://doi.org/10.1016/j.buildenv.2016.04.028.
[52] L.W. Chew, L.R. Glicksman, L.K. Norford, Buoyant flows in street canyons: comparison of RANS and LES at reduced and full scales, Build. Environ. 146 (2018) 77–87, https://doi.org/10.1016/j.buildenv.2018.09.026.
[53] P.-Y. Cui, J.-Q. Wang, F. Yang, Q.-X. Zhao, Y.-D. Huang, Y. Yang, W.-Q. Tao, Effects of radiant floor heating integrated with natural ventilation on flow and dispersion in a newly decorated residence, Int. J. Environ. Res. Publ. Health 19 (2022) 16889, https://doi.org/10.3390/ijerph192416889.
[54] D.W. Etheridge, M. Sandberg, A simple parametric study of ventilation, Build. Environ. 19 (1984) 163–173, https://doi.org/10.1016/0360-1323(84)90023-4.
[55] P.V. Nielsen, Flow in Air Conditioned Rooms: Model Experiments and Numerical Solution of the Flow Equations, 1974.
[56] J.S. Zhang, G.J. Wu, L.L. Christianson, A New Similitude Modelling Technique for Studies of Non Isothermal Room Ventilation Flows, 1993.
[57] J. Park, X. Sun, J.-I. Choi, G.H. Rhee, Effect of wind and buoyancy interaction on single-sided ventilation in a building, J. Wind Eng. Ind. Aerod. 171 (2017) 380–389, https://doi.org/10.1016/j.jweia.2017.10.016.
[58] Y. Hwang, C. Gorlé, Large-eddy simulations to define building-specific similarity relationships for natural ventilation flow rates, Flowline 3 (2023) E10, https://doi.org/10.1017/flo.2023.4.
[59] S.-J. Mei, C. Yuan, Urban buoyancy-driven air flow and modelling method: a critical review, Build. Environ. 210 (2022) 108708, https://doi.org/10.1016/j.buildenv.2021.108708.
[60] C. Bibby, M. Hodgson, V. Vasudevan Shankar, Applicability of flow-rate-independent discharge coefficients in purpose-provided, interior natural-ventilation openings, Int. J. Vent. 17 (2018) 31–47, https://doi.org/10.1080/14733315.2017.1351735.
[61] Z. Jiang, T. Kobayashi, T. Yamanaka, M. Sandberg, N. Choi, N. Kobayashi, K. Sano, K. Toyosawa, Wind-induced ventilation rate of single-sided ventilation in a building with internal partition, Int. J. Vent. 0 (2024) 1–22, https://doi.org/10.1080/14733315.2024.2319475.
[62] A.G. Davenport, The application of statistical concepts to the wind loading of structures, Proc. Inst. Civ. Eng. 19 (1961) 449–472, https://doi.org/10.1680/iicep.1961.11304.
[63] J. Wieringa, Updating the Davenport roughness classification, J. Wind Eng. Ind. Aerod. 41 (1992) 357–368, https://doi.org/10.1016/0167-6105(92)90434-C.
[64] Y. Tominaga, A. Mochida, R. Yoshie, H. Kataoka, T. Nozu, M. Yoshikawa, T. Shirasawa, AIJ guidelines for practical applications of CFD to pedestrian wind environment around buildings, J. Wind Eng. Ind. Aerod. 96 (2008) 1749–1761, https://doi.org/10.1016/j.jweia.2008.02.058.
[65] M. Darwish, I. Sraj, F. Moukalled, A coupled finite volume solver for the solution of incompressible flows on unstructured grids, J. Comput. Phys. 228 (2009) 180–201, https://doi.org/10.1016/j.jcp.2008.08.027.
[66] B.P. Leonard, S. Mokhtari, ULTRA-SHARP Nonoscillatory Convection Schemes for High-Speed Steady Multidimensional Flow, 1990.
[67] B.A. Kader, Temperature and concentration profiles in fully turbulent boundary layers, Int. J. Heat Mass Tran. 24 (1981) 1541–1544, https://doi.org/10.1016/0017-9310(81)90220-9.
[68] S. Michael, O. Helge, F. Jörg, COST 732 Model Evaluation Case Studies: Approach and Results, University of Hamburg, 2010.

[69] W.P. Jones, B.E. Launder, The prediction of laminarization with a two-equation model of turbulence, Int. J. Heat Mass Tran. 15 (1972) 301–314, https://doi.org/10.1016/0017-9310(72)90076-2.
[70] F.R. Menter, Two-equation eddy-viscosity turbulence models for engineering applications, AIAA J. 32 (1994) 1598–1605, https://doi.org/10.2514/3.12149.
[71] A. Fluent, Ansys Fluent Theory Guide, vol. 15317, Ansys Inc., USA, 2011, pp. 724–746.
[72] Y. Tominaga, T. Stathopoulos, CFD simulations of near-field pollutant dispersion with different plume buoyancies, Build. Environ. 131 (2018) 128–139, https://doi.org/10.1016/j.buildenv.2018.01.008.
[73] P.F. Crapper, W.D. Baines, Some remarks on non-boussinesq forced plumes, Atmos. Environ. 12 (1967) 1939–1941, https://doi.org/10.1016/0004-6981(78)90128-2, 1978.
[74] Y. Zhou, M. Wang, M. Wang, Y. Wang, Predictive accuracy of Boussinesq approximation in opposed mixed convection with a high-temperature heat source inside a building, Build. Environ. 144 (2018) 349–356, https://doi.org/10.1016/j.buildenv.2018.08.043.
[75] P.-Y. Cui, Z. Li, W.-Q. Tao, Numerical investigations on *Re*-independence for the turbulent flow and pollutant dispersion under the urban boundary layer with some experimental validations, Int. J. Heat Mass Tran. 106 (2017) 422–436, https://doi.org/10.1016/j.ijheatmasstransfer.2016.08.038.
[76] Architectural Institute of Japan, Guidebook for CFD Predictions of Urban Wind Environment, 2020.
[77] H.B. Awbi, M.M. Nemri, Scale effect in room air movement modelling, in: Roomvent 90, Norway, 1990. Oslo.
[78] L.W. Chew, Buoyancy-driven natural ventilation: the role of thermal stratification and its impact on model accuracy, E3S Web of Conf. 396 (2023) 02038, https://doi.org/10.1051/e3sconf/202339602038.
[79] D.W. Etheridge, J.A. Nolan, Ventilation measurements at model scale in a turbulent flow, Build. Environ. 14 (1979) 53–64, https://doi.org/10.1016/0360-1323(79)90029-5.
[80] D. Wu, R. Burton, G. Schoenau, An empirical discharge coefficient model for orifice flow, Int. J. Fluid Power 3 (2002) 13–19, https://doi.org/10.1080/14399776.2002.10781143.
[81] H.E. Merritt, Hydraulic Control Systems, J. Wiley, 1967 n.d.